


Cite this: *RSC Adv.*, 2017, 7, 24263

# Synthesis, growth mechanism, optical properties and catalytic activity of ZnO microcrystals obtained via hydrothermal processing

Edgar Alves Araújo Júnior,<sup>†a</sup> Francisco Xavier Nobre,<sup>†b</sup> Giancarlo da Silva Sousa,<sup>a</sup> Laécio Santos Cavalcante,<sup>c</sup> Maria Rita de Moraes Chaves Santos,<sup>a</sup> Flavio Leandro Souza<sup>†d</sup> and José Milton Elias de Matos <sup>†\*a</sup>

In the present study, typical ZnO microcrystals exhibiting the wurtzite hexagonal crystal structure were produced successfully, characterized by a high degree of crystallinity, via hydrothermal processing at 120, 150 and 180 °C, assisted by *N*-cetyl-*N,N,N*-trimethylammonium (CTAB). The samples were characterised by XRD, Raman and infrared, FE-SEM, UV-Vis by diffuse reflectance and photoluminescence (PL). The experimental results confirm that all hydrothermally synthesised ZnO samples were crystallised into a wurtzite hexagonal structure. The ZnO crystals exhibit the morphology of hexagonal columns in the absence and double hexagonal columns in the presence of CTAB. The length and average diameter of the microstructures decrease with increasing processing temperature. It is evident that all the synthesised samples present very similar profiles and band positions in the PL emission spectra, with an emission band in the violet range at approximately 400 nm, a small peak in the UV range at approximately 380 nm, and highly superposed and intense emission bands between 440 and 750 nm (blue to red emission), with a maximum at approximately 610 nm. Furthermore, a nucleation and growth model was proposed to explain the formation of ZnO microcrystals, based on the experimental conditions, that were preferably grown in the [001] direction. In addition, the ZnO exhibited excellent performance in the photocatalytic degradation of rhodamine B (RhB) and methyl orange (MO), achieving 97% and 99% photodegradation of RhB and MO, respectively, when ZnO obtained at 120 °C, in the absence of CTAB, was used as catalyst.

Received 20th March 2017

Accepted 26th April 2017

DOI: 10.1039/c7ra03277c

rsc.li/rsc-advances

## 1. Introduction

Zinc oxide (ZnO) is a semiconductor material with a wide band gap (3.37 eV), large exciton binding energy (60 meV) and singular electronic and optical properties that are particularly affected by the morphology and size of the crystals.<sup>1,2</sup> Studies have demonstrated the versatility and potential capability of ZnO for a wide range of applications in photonic, photovoltaic and electronic devices, such as light-emitting diodes (LEDs), lasers, UV detectors, transistors and solar cells.<sup>3–9</sup> ZnO also

exhibits interesting piezoelectric properties that permit its application as transducers and surface acoustic wave (SAW) and bulk acoustic wave (BAW) devices.<sup>10,11</sup> Furthermore, especially in the form of powder, ZnO can be applied to pigments,<sup>12</sup> photo(catalysts),<sup>13,14</sup> and UV radiation attenuators.<sup>15</sup> Because of its excellent UV attenuation properties, ZnO can also be used in cosmetics, paints, varnish and plastics.<sup>10,16,17</sup> In the last five year, ZnO has gained especial attention as antimicrobial agent<sup>5,18</sup> and in cancer therapy due it ability to distinguish between normal and cancers cells.<sup>19,20</sup> Additionally, ZnO can be used as an antimicrobial agent.<sup>5,18</sup>

Powder ZnO can be synthesised using various synthesis methods that are well established in the literature, such as zinc oxidation from metallic zinc vapour, through the French or American process,<sup>21</sup> decomposition of salts containing zinc,<sup>22</sup> spray pyrolysis,<sup>23</sup> sol-gel<sup>24,25</sup> and coprecipitation.<sup>26,27</sup> Most of these methods employ high temperatures up to 1000 °C to crystallise the ZnO phase. In such cases, the high processing temperatures lead to the excessive formation of aggregates in the ZnO powder, which results in little control over the morphology and particle size distribution.<sup>10</sup>

<sup>a</sup>Interdisciplinary Laboratory of Advanced Materials, LIMAV, Natural Sciences Centre, CCN, Department of Chemistry, Federal University of Piauí, Teresina, Piauí, 64049-550, Brazil. E-mail: jmematos@ufpi.edu.br; Tel: +55-086-3215-5840

<sup>b</sup>Laboratory of Research in Biology and Chemistry, LPBQ, Campus Coari, Federal Institute of Amazonas, IFAM, Road Coari-Itapêua, Coari, Itamaraty, AM, 69067-360, Brazil. Tel: +55-097-3561-2470

<sup>c</sup>GERATEC, Natural Sciences Centre (Centro de Ciências da Natureza), University of State of Piauí (Universidade Estadual do Piauí), Teresina, Piauí, 64002-150, Brazil

<sup>d</sup>Natural and Human Sciences Centre (Centro de Ciências Naturais e Humanas – CCNH), Federal University of ABC (Universidade Federal do ABC), 09210-170 Santo André, SP, Brazil

<sup>†</sup> These authors contributed equally to this work.



In turn, the hydrothermal processing crystallises anhydrous materials directly from aqueous solutions at temperatures higher than room temperature, usually between 100 and 300 °C, and pressures higher than normal pressures to obtain a fine powder under the corresponding saturated water vapour pressures.<sup>28</sup> Among the various physical and chemical material preparation methodologies (bottom-up), the chemical method for material preparation from an aqueous solution maintained at hydrothermal conditions offers numerous advantages to large-scale production such as: (i) the performance of single-stage synthesis, with no subsequent calcination and grinding; (ii) low aggregation level, (iii) narrow crystallite size distribution; and (iv) high purity with excellent control of morphology and particle size.<sup>6,29</sup> This method offers many advantages over the conventional synthesis methods, such as the performance of single-stage synthesis, with no subsequent calcination and grinding, a low aggregation level and a narrow crystallite size distribution, as well as high purity and excellent control of the morphology and particle size.<sup>6,29</sup> The hydrothermal processing conditions often result in chemical structures with unique structure defects that cannot be generated using the classical methods, which use very high processing temperatures; therefore, these conditions can result in materials with exclusive properties.<sup>30,31</sup> The processing is called solvothermal when water is not used as the solvent and presents the same advantages as the hydrothermal processing method.<sup>32</sup> Solvothermal synthesis of materials is normally used when there is the need for strict control of the particle size and shape and avoids premature agglomeration. However, from the economical viewpoint, the synthesis processes at hydrothermal conditions (water as the solvent) involve simpler equipment and fast and efficient residue removal compared with the process performed exclusively in organic solvents.

For instance, control nanomaterial size and morphology has been intensively investigated in terms of photocatalysis application. Among several materials for this purpose ZnO and TiO<sub>2</sub> are two of the most popular photocatalysts used for organic pollutant degradation,<sup>33–35</sup> water waste treatment,<sup>36–39</sup> clean fuel production<sup>40–42</sup> and so on. Adhikari *et al.*, showed an effective degradation of methyl orange under visible light irradiation by using a quasi-fibrous morphology of ZnO powder synthesized by combustion process.<sup>43</sup> Fang and coworkers<sup>44</sup> compared the performance on methyl orange photodegradation using sphere and flower-like ZnO morphology obtained at temperature below 200 °C under hydrothermal condition. The spherical ZnO morphology resulted in a superior photocatalytic activity compared with flower-like ZnO and commercial ones, which was attributed to a higher specific area and existence of more available oxygen vacancies.<sup>44</sup> More recently, Wolski *et al.*<sup>45</sup> demonstrated that the high surface area provided by the spherical zinc oxide morphology is less important than crystallinity degree and defect density towards the photodegradation efficiency of rhodamine B. Therefore, a sufficient area should be required to guarantee the total photodegradation of the rhodamine B, otherwise only partial conversion of the pollutant can be reach in a short period of irradiation. Indeed, the photocatalytic activity is governates by

a compromise in between synthetic method and final properties by a fine control of several parameters such as, size, morphology, surface area, defect density, *etc.* Based on the literature report history seems that the key factor for higher photocatalytic activity is not the same for the available materials, which open avenues for intensive and detailed investigation in this field to achieve a better method and material for this application.<sup>8–45</sup>

In the present study, surfactant-assisted hydrothermal processing was applied for the synthesis of ZnO microcrystals at mild temperatures. The *N*-cetyl-*N,N,N*-trimethylammonium bromide (CTAB) cationic tensioactive has been used in hydrothermal synthesis to favour the growth and orientation of ZnO crystals,<sup>46</sup> and in this study, its effect on the morphology and size of ZnO microcrystals is investigated. The ZnO wurtzite phase is not centrosymmetric, as it exhibits polar crystalline faces,<sup>47</sup> which is significant for crystal growth. For various applications, the structure of ZnO should be investigated, and its growth behaviour should be controlled. The growth pattern, size and morphology of the ZnO crystal structures obtained by the hydrothermal method are usually affected by the pH, presence of additives, processing temperature and concentration of reagents.<sup>48</sup> We also evaluated the photocatalytic activity of ZnO in degradation of rhodamine B (RhB) and methyl orange (MO) under visible light irradiation.

## 2. Experimental

### 2.1. ZnO synthesis by the hydrothermal method

The ZnO crystals were synthesised by the hydrothermal method in alkaline medium. The starting materials were as follows: zinc acetate dihydrate (ZAD) [Zn(CH<sub>3</sub>COO)<sub>2</sub>·2H<sub>2</sub>O] (>98%, Vetec), sodium hydroxide [NaOH] (97%, Sigma-Aldrich), CTAB [C<sub>19</sub>H<sub>42</sub>BrN] (>99%, Vetec) and distilled water. All the reagents were of analytical grade and were used with no previous purification.

Approximately 6.0 g of ZAD and 4.5 g of CTAB were weighed and transferred to stainless steel-coated polytetrafluoroethylene (PTFE) autoclaves with screw lids. Next, 100 mL of 0.3 M NaOH solution was added, and manual agitation was performed using a glass stirring rod for 10 min. Then, the autoclaves were sealed with proper lids and transferred to an oven (Quimis, Q819V), where they remained for 24 h at different temperatures (120, 150 and 180 °C). After the reaction period, the solutions were washed with distilled water and ethyl alcohol (95%, Vetec) in a centrifuge (Sigma, 3-16L) at 3000 rpm. The samples were dried in an oven (Odontobras, EL 1.1) at 75 °C for approximately 8 h.

### 2.2. Characterisation

The samples were characterised by X-ray diffraction (XRD) using a Shimadzu diffractometer, model XRD6000 (Japan) using Cu-K $\alpha$  radiation ( $\lambda = 1.54056 \text{ \AA}$ ) at 40 kV and 30 mA. The tests were performed with a step size of 0.02° between 10 and 110° ( $2\theta$ ) with a scan rate of 0.5° per minute in continuous mode. The XRD patterns of the samples were refined using the Rietveld method using the DBWSTools program. The refinement



procedure consisted primarily of adjusting the displacement parameters of the sample relative to the crystal plane, background, scale factor, full-width at half-maximum of the diffraction peak ( $W$ ), asymmetry factor, peak profile (NA and NB), lattice parameters ( $a$ ,  $b$ ,  $c$ ;  $\alpha$ ,  $\beta$ ,  $\gamma$ ), possible preferential orientation, atomic positions ( $x$ ,  $y$ ,  $z$ ), isotropic or anisotropic thermal parameters, and instrumental parameters ( $U$  and  $V$ ). The special atomic positions were not refined as they are intrinsic parameters of the sample.

The Raman spectra were collected using a Bruker Senterra monochromator (Germany) coupled to an Olympus BX50 microscope, connected to a CCD (charge-coupled device) detector, with automatic resolution adjustment at  $0.1 \text{ cm}^{-1}$ . The readings were performed at room temperature from 35 to  $1555 \text{ cm}^{-1}$  using a laser with an excitation wavelength of 532 nm, with output power of 20 mW and an integration time of 10 s. The measurements in the infrared (IR) region were obtained using a Bruker spectrometer, model Vertex 70 (Germany) in the range from  $4000$  to  $400 \text{ cm}^{-1}$ , with 32 scans for each measurement and a resolution of  $4 \text{ cm}^{-1}$ .

The morphology of the ZnO particles was investigated using field-emission scanning electron microscopy (FE-SEM) using an FE-SEM-FEI microscope, model Inspec F-50. From the FE-SEM images, the particle size distribution was estimated, and the morphology was examined.

Diffuse reflectance ( $R$ ) UV-Vis spectra were registered using a Varian spectrophotometer, model Cary 5G (United States), with wavelengths ranging between 200 and 800 nm. Magnesium oxide (MgO) was used as the reference material, and a special sample holder was adapted for powders. The photoluminescence (PL) measurements were performed in a Monospec 27 monochromator from Thermal Jarrel Ash (United States), coupled to a R446 photomultiplier from Hamamatsu Photonics (Japan), with an SR-530 lock-in acquisition system. A krypton ion laser of 350.7 nm from Coherent Innova 90 K (United States) was used as the excitation source, maintaining its maximum power at 200 mW.

### 2.3. Photocatalytic activity

The photocatalytic experiments were conducted using 100 mL of dye solution (RhB and MO) at a concentration of  $1.0 \times 10^{-5} \text{ mol L}^{-1}$ , added in a quartz reactor 600 mL under magnetic stirring and an average temperature of  $25.0 \pm 0.5 \text{ }^\circ\text{C}$ . Subsequently, inserted for each catalytic test, 100 mg of the catalyst, which remained under magnetic stirring for 5 minutes, followed by stirring in an ultrasound tub Cristófoli mark A52243ZZZ110V code, with a frequency of 42 kHz for 10 minutes in order to obtain the adsorption equilibrium in solution. The emulsion obtained was inserted in a photocatalytic system consisting of a wooden box with two coupled microfan (1.5 A and 12 V), six UVC lamps (Osram 15 W) with a wavelength of 253.7 nm, a magnetic stirrer and an aquarium pump with a flow rate of  $1.8 \text{ L min}^{-1}$ . The monitoring of catalytic activity was carried out by removing 4 mL of the solution followed by centrifugation of 5000 rpm for 10 minutes, analyzing the wavelength of maximum absorption of the supernatant, the

latter being 554 nm and 465 nm, corresponding to RhB dyes and MO, respectively. Operating a spectrophotometer brand Thermo Scientific GENESYS 10S model, conducting sweeps in the range of 200 nm to 900 nm, with  $10 \text{ nm s}^{-1}$  by adding solutions in quartz cuvettes.

## 3. Results and discussion

### 3.1. XRD and Rietveld refinement

Fig. 1 presents the diffractograms of the ZnO microcrystals synthesised by the hydrothermal method for 24 h at 120, 150 and  $180 \text{ }^\circ\text{C}$ , with and without the assistance of CTAB. The position of the peaks in all the diffractograms presented in Fig. 1 have the same pattern, regardless of the preparation conditions of the ZnO powder. This pattern confirms that the crystal structure of the samples is hexagonal (wurtzite), with  $C_{6v}^4$  or  $P6_3mc$  spatial group and crystallographic class 6 mm, according to the respective crystallographic card ICSD no. 34477 (ICSD = Inorganic Crystal Structure Database).<sup>49</sup> Intermediate crystal phases were not observed, indicating the high purity of these materials obtained in a single stage at hydrothermal conditions. The presence of defined and intense peaks indicates that the ZnO powders exhibit high crystallinity (structural periodicity) and are structurally ordered at a long distance.

Once the crystallography phase ZnO was confirmed, the XRD results underwent the refinement process by the Rietveld method using the DBWS Tools software interface. The data on crystallographic pattern profiles of the wurtzite phase is available on the Capes Research Website<sup>50</sup> from the International Center for Diffraction Data (ICDD). The ICSD no. 34477 (ref. 49) card was used.

Table 1 presents the lattice parameters and the unit cell volume of the ZnO samples, which were calculated after the structural refinement and compared with the data reported in the literature.<sup>51–57</sup> The slight variations on the experimental

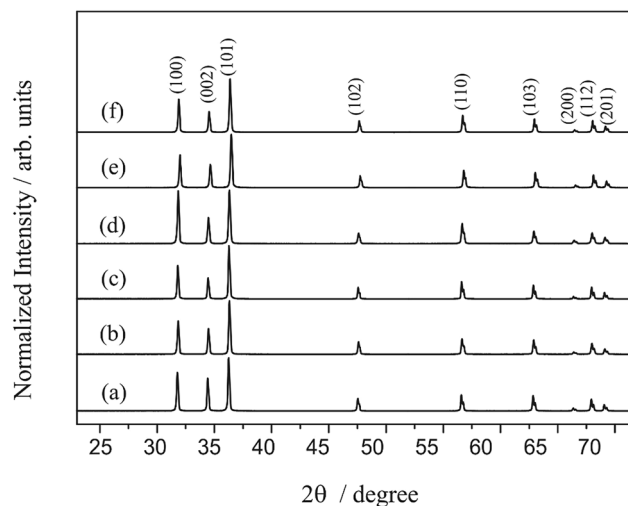


Fig. 1 XRD patterns of ZnO synthesized hydrothermally for 24 h at  $120 \text{ }^\circ\text{C}$  (a) without and (b) with CTAB, at  $150 \text{ }^\circ\text{C}$  (c) without and (d) with CTAB, and at  $180 \text{ }^\circ\text{C}$  without (e) and (f) with CTAB.



**Table 1** Comparative results between the lattice parameters and unit cell volume of the hydrothermally processed ZnO microcrystals in this study, with data reported in the literature, using different synthesis methods and information on bulks<sup>a</sup>

		Lattice parameters (Å)				JCPDS	Ref.
<i>T</i> (°C)	<i>t</i> (h)	<i>a</i> = <i>b</i>	<i>c</i>	<i>V</i> (Å <sup>3</sup> )			
<b>Synthesis methods</b>							
HT	140	24	0.3249	0.5206	—	36-1451	32
HT	150	24	0.3249	0.5206	—	36-1451	51
HT	140	12	0.3242	0.5188	—	79-0205	52
SG	80	24	0.324	0.519	54.5	36-1451	24
HT	140	12	0.3251	0.5206	—	79-2205	53
HT	180	24	0.3249	0.5205	—	75-0576	46
HT	120	5	0.32508	0.52069	—	36-1451	54
CP	60	2	0.3250	0.5207	—	36-1451	55
<b>Bulks</b>							
		Lattice parameters (Å)				JCPDS	Ref.
		<i>a</i> = <i>b</i>	<i>c</i>	<i>V</i> (Å <sup>3</sup> )			
<b>BK - ICSD no. 26170</b>							
		0.32498	0.52066	47.623	—	56	
<b>BK - ICSD no. 34477</b>							
		0.3253	0.5213	47.77	—	49	
<b>BK - ICSD no. 57450</b>							
		0.32494	0.52038	47.59	—	59	
<b>This study</b>							
		Lattice parameters (Å)				JCPDS	CTAB
<i>T</i> (°C)	<i>t</i> (h)	<i>a</i> = <i>b</i>	<i>c</i>	<i>V</i> (Å <sup>3</sup> )			
HT	120	24	0.3251	0.5207	47.66	36-1451	No
HT	120	24	0.3252	0.5207	47.70	36-1451	Yes
HT	150	24	0.3252	0.5209	47.70	36-1451	No
HT	150	24	0.3250	0.5208	47.65	36-1451	Yes
HT	180	24	0.2513	0.5209	47.69	36-1451	No
HT	180	24	0.3250	0.5207	47.64	36-1451	Yes

<sup>a</sup> *T* = temperature; *t* = processing time; *a*, *b*, *c* = lattice parameters; *V* = unit cell volume; JCPDS = Joint Committee on Powder Diffraction Standards; ICSD = Inorganic Crystal Structure Database; Ref. = reference; pH = pH value; CT = presence or absence of CTAB (cetyl trimethylammonium bromide); N = no; Y = yes; HT = hydrothermal; SG = sol-gel; CP = coprecipitation; BK = bulk.

results may be related to the different types of synthesis methods and experimental conditions, such as the processing temperature, heating rate, reaction time, atmosphere, solvent, *etc.*, which, consequently, may generate different levels of long-range structural organisation in the hexagonal lattice.

The complete results of the structural refinement by the Rietveld method are presented in Table 2, with the following Rietveld refinement results: density and unit cell volume, atomic positions (*x*, *y*, *z*) and refinement quality indexes (*R<sub>p</sub>*, *R<sub>wp</sub>*, *R<sub>exp</sub>*, and *S*). Table 2 presents the numerical quality indicators of structural refinement using the Rietveld method. *S* parameter values smaller than 2 indicate satisfactory refinement;<sup>58</sup> the samples maintained at 180 °C in hydrothermal conditions exhibited values of *S* = 1.88 and 1.95, with and without the assistance of CTAB, respectively.

**Table 2** Atomic coordinates obtained from the Rietveld refinement data for ZnO crystals synthesised for 24 h at 120, 150 and 180 °C, with and without the assistance of CTAB

Atoms	Wyckoff	Sites	<i>x</i>	<i>y</i>	<i>z</i>
<b>120 °C, CTAB: no</b>					
Zinc	2b	3m	0.3333	0.6667	0
Oxygen	2b	3m	0.3333	0.6667	0.3917
Density = 5.667 g cm <sup>-3</sup> ; <i>R<sub>p</sub></i> = 9.56%; <i>R<sub>wp</sub></i> = 12.28%; <i>R<sub>exp</sub></i> = 5.14% and <i>S</i> = 2.39					
<b>120 °C, CTAB: yes</b>					
Zinc	2b	3m	0.3333	0.6667	0
Oxygen	2b	3m	0.3333	0.6667	0.3857
Density = 5.674 g cm <sup>-3</sup> ; <i>R<sub>p</sub></i> = 7.06%; <i>R<sub>wp</sub></i> = 10.15%; <i>R<sub>exp</sub></i> = 5.29% and <i>S</i> = 1.92					
<b>150 °C, CTAB: no</b>					
Zinc	2b	3m	0.3333	0.6667	0
Oxygen	2b	3m	0.3333	0.6667	0.3818
Density = 5.667 g cm <sup>-3</sup> ; <i>R<sub>p</sub></i> = 7.45%; <i>R<sub>wp</sub></i> = 11.12%; <i>R<sub>exp</sub></i> = 5.28% and <i>S</i> = 2.10					
<b>150 °C, CTAB: yes</b>					
Zinc	2b	3m	0.3333	0.6667	0
Oxygen	2b	3m	0.3333	0.6667	0.3960
Density = 5.674 g cm <sup>-3</sup> ; <i>R<sub>p</sub></i> = 12.37%; <i>R<sub>wp</sub></i> = 14.96%; <i>R<sub>exp</sub></i> = 5.04% and <i>S</i> = 2.96					
<b>180 °C, CTAB: no</b>					
Zinc	2b	3m	0.3333	0.6667	0
Oxygen	2b	3m	0.3333	0.6667	0.3806
Density = 5.669 g cm <sup>-3</sup> ; <i>R<sub>p</sub></i> = 6.95%; <i>R<sub>wp</sub></i> = 10.53%; <i>R<sub>exp</sub></i> = 5.59% and <i>S</i> = 1.88					
<b>180 °C, CTAB: yes</b>					
Zinc	2b	3m	0.3333	0.6667	0
Oxygen	2b	3m	0.3333	0.6667	0.3812
Density = 5.674 g cm <sup>-3</sup> ; <i>R<sub>p</sub></i> = 7.02%; <i>R<sub>wp</sub></i> = 10.42%; <i>R<sub>exp</sub></i> = 5.34% and <i>S</i> = 1.95					

The Rietveld refinement calculations for the ZnO microcrystals hydrothermally processed at 180 °C, with and without the assistance of CTAB, are presented in Fig. 2. The results indicate good agreement between the profiles of the experimental diffractograms and the theoretical data for the ZnO wurtzite structure. The differences between the diffractogram profiles (*Y<sub>observed</sub>* - *Y<sub>calculated</sub>*) are small on the scale of intensity.

In turn, the samples synthesised at 120 and 150 °C, in the presence and absence of CTAB, exhibited high *S* values because *R<sub>exp</sub>* was smaller. Nevertheless, the refinements can be considered of good quality, as the value of *R<sub>exp</sub>* is lower because of the high intensities. Consequently, the value of *S* becomes higher than 2 for such cases, which also has been reported in literature (ex.: *S* = 3.31).<sup>59</sup>

According to Young,<sup>60</sup> although the numerical indicators are important for the refinements by maximum likelihood, it is vital to perform the graph fitting analysis by the line of differences between the observed and calculated data.



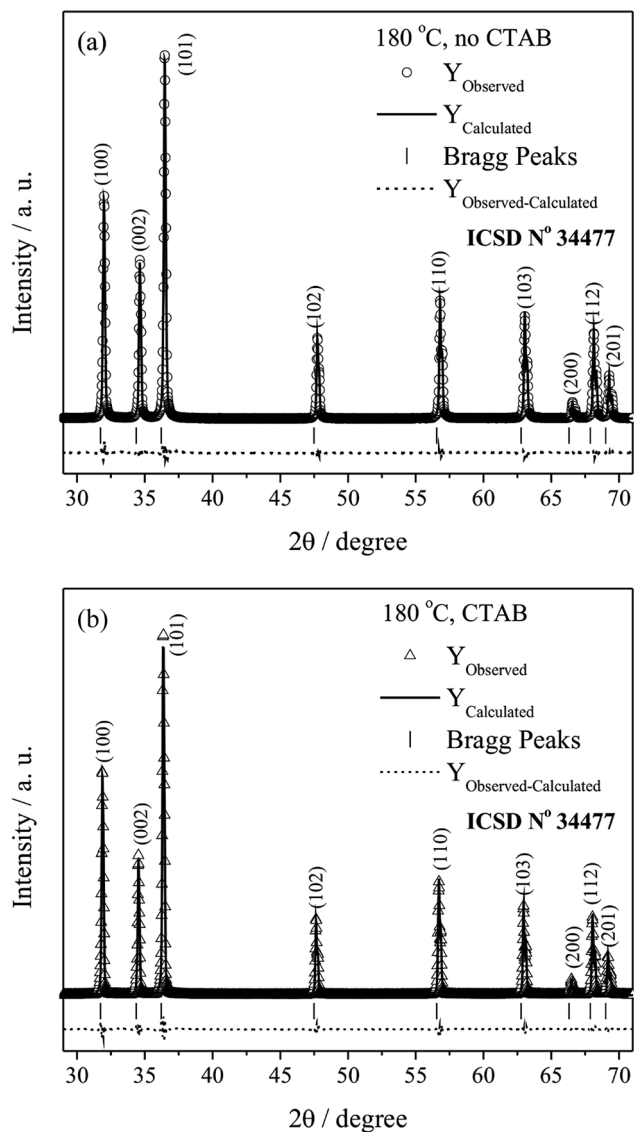


Fig. 2 XRD pattern refinements using the Rietveld method of ZnO, (a) without and (b) with the assistance of CTAB, at 180 °C.

### 3.2. Unit cells representation

Fig. 3 presents schematic representations for the unit cells of the ZnO microcrystals hydrothermally processed at 180 °C for 24 h, with and without the assistance of CTAB, from the structural refinement data obtained using the Rietveld method. The unit cells were modelled using the Diamond Crystal and Molecular Structure Visualisation program, demo version 3.2f for Windows,<sup>61</sup> using the atomic coordinates calculated by the Rietveld refinement, displayed in Table 2.

Some interesting characteristics are observed in the unit cells presented in Fig. 3, such as: (i) the unit cell contains four atoms, two of each type (Zn and O); each atom is tetrahedrally coordinated in the crystal lattice, with hexagonal symmetry; and (ii) the two types of atoms occupy a sublattice throughout the *c* axis. In fact, this type of structure is composed by two compact hexagonal sublattices, where the layers occupied by Zn atoms

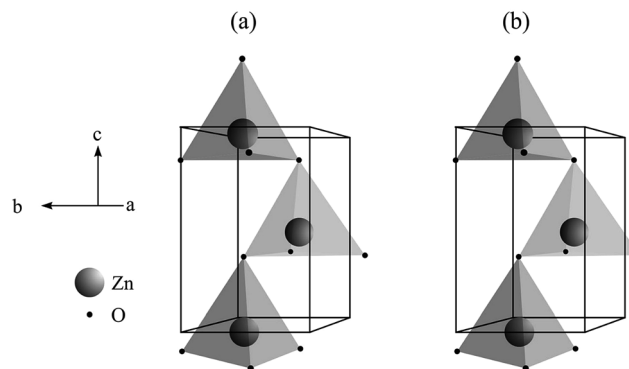


Fig. 3 Modeling of unit cells of ZnO microcrystals synthesized hydrothermally at 180 °C, for 24 h (a) without and (b) with CTAB.

alternate with the layers occupied by O atoms around the *c* axis. In every sublattice, four atoms are included per unit cell, for instance, each Zn atom is coordinated to four O atoms, or *vice versa*. Hence, half of the tetrahedral sites are occupied by Zn atoms.

The unit cell volume is approximately 47.6 Å<sup>3</sup>. Consequently, ZnO contains approximately  $8.4 \times 10^{22}$  atoms per cm<sup>3</sup>. The synthetically produced ZnO with the wurtzite structure may eventually exhibit a crystallographic arrangement different from the pattern established in the crystallographic records. A characteristic of this type of hexagonal crystalline arrangement is the *c/a* ratio between the unit cell parameters, which was determined to be 1.63 for the ideal arrangement, considering the atomic positions (*x*, *y*, *z*) and maximum packing.<sup>62</sup> Generally, the main reasons that the synthetic materials differ from the ideal arrangement are related to the methodology of preparation, which depends on external factors such as the pressure and temperature, time, and presence of impurities, among others.<sup>62</sup> In the real ZnO crystal, the wurtzite structure diverges from the ideal arrangement because the *c/a* ratio varies. Although the ideal wurtzite structure exhibits a *c/a* ratio of 1.63,<sup>62</sup> the lattice constants of the real ZnO structure depend on impurities, external factors, temperature, *etc.*

### 3.3. Raman and IR spectroscopy

The structural lattice of the ZnO wurtzite phase consists of a basic unit of four atoms per unit cell (two Zn–O molecular units). Because of the number  $n = 4$  atoms in the unit cell, the number of phonons is equivalent to  $3n = 12$ , with 3 acoustic modes (1 × LA, 2 × TA) and  $3n - 3 = 9$  optical phonons (3 × LO, 6 × TO). In the  $\Gamma$  point of the Brillouin zone, the optical phonons have irreducible representation:

$$\Gamma(\text{Raman} + \text{infrared}) = 1A_1 + 2B_1 + 1E_1 + 2E_2, \quad (1)$$

whereas the E modes are doubly degenerated. The  $B_1$  modes are silent modes, *i.e.*, inactive in the Raman and infrared spectra, and the  $E_2$  modes are only active in the Raman spectra. Modes  $A_1$  and  $E_1$ , active in the Raman and infrared spectra, are polar. Therefore, each one is divided into longitudinal (LO) and



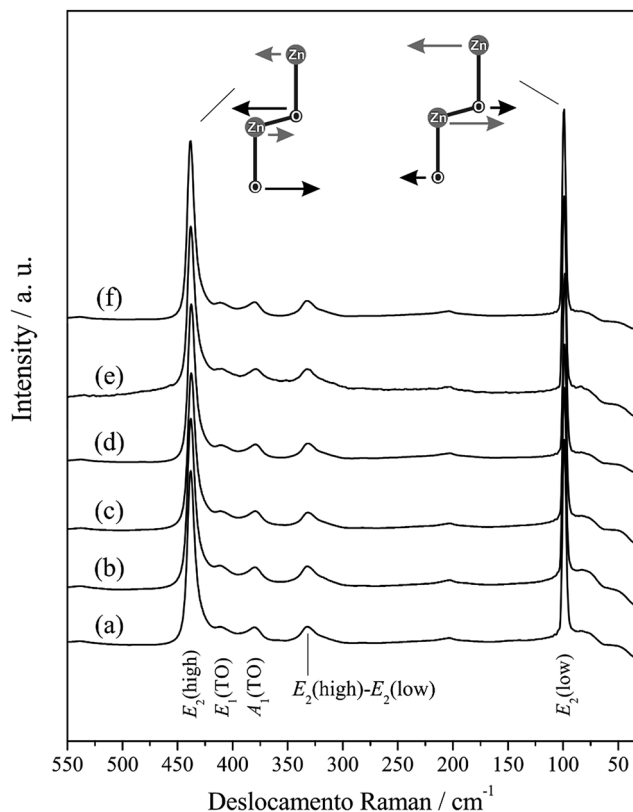


Fig. 4 Raman spectra of ZnO processed hydrothermally for 24 h at 120 °C (a) without and (b) with CTAB, at 150 °C (c) without and (d) with CTAB and 180 °C without (e) and (f) CTAB. The  $E_2$  modes(low) and  $E_2$ (high) are shown in figure.

transversal (TO) optical modes caused by macroscopy electric field of phonons localized at LO, which are represented by the Raman mode in the range of wavenumber from 98 to 591  $\text{cm}^{-1}$ .

Fig. 4 presents the Raman spectra for the ZnO microcrystals synthesised for 24 h at 120, 150 and 180 °C, with and without the assistance of CTAB. The band position, attribution and main Raman modes reported in the literature of ZnO crystals obtained by different synthesis, bulk and theoretical methods are listed in Table 3.<sup>5,11,16,26,63-73</sup>

The modes present in the Raman spectra of the ZnO samples investigated in this study were attributed to the wurtzite crystal structure. The intense  $E_2$ (low) band, approaching 100  $\text{cm}^{-1}$ , is attributed to the vibrations of the Zn sublattice in the ZnO structure. The bands close to 330 and 380  $\text{cm}^{-1}$  are attributed to modes  $E_2$ (high) –  $E_2$ (low) (second-order acoustic) and  $A_1$ (TO), respectively. Almost unnoticeable, the weak band approaching 200  $\text{cm}^{-1}$  refers to mode  $2E_2$ (low). An evident and strong peak is present in all the spectra at approximately 440  $\text{cm}^{-1}$ , which is characteristic of the scattering of the ZnO hexagonal wurtzite dominant mode  $E_2$ (high) and is attributed to the vibration of the sublattice of O. Additionally, the literature reports that mode  $E_2$ (high) exhibits excellent crystallinity<sup>74</sup> and acts as a signature of the ZnO wurtzite phase, which demonstrates the good correlation with the XRD data for all the ZnO microcrystals synthesised at hydrothermal conditions.

Table 3 Comparison among the main Raman active modes for ZnO crystals obtained in this study and other studies reported in the literature obtained by different synthesis, bulk and theoretical methods<sup>a</sup>

	$T$ (°C)	$t$ (h)	Modes*				Ref.
			$A_1$ (TO)	$E_1$ (TO)	$E_2$ (low)	$E_2$ (high)	
<b>Synthesis methods</b>							
CL	400	2	380	—	99	438	63
ET	900	1	380	407	101	437	64
SG	550	2	380	414	—	440	65
SG	750	2	380	—	—	435	66
CP	120	2	380	418	—	438	26
HT	120	72	382	409	102	440	5
HT	130	24	381	—	—	438	11
HT	80	20	385	—	—	439	67
HT	200	10	383	—	—	438	16
MH	130	3	378	—	—	437	68
<b>Bulks</b>							
BK	—	—	379	410	102	437	69
BK	—	—	380	407	101	437	70
BK	—	—	380	413	101	444	71
<b>Theoretical</b>							
TR	—	—	386	407	98	433	72
TR	—	—	382	316	126	335	73

	$T$ (°C)	$t$ (h)	Modes*				CTAB
			$A_1$ (TO)	$E_1$ (TO)	$E_2$ (low)	$E_2$ (high)	
<b>This study</b>							
HT	120	24	380	411	99	438	No
HT	120	24	380	412	99	438	Yes
HT	150	24	380	411	99	438	No
HT	150	24	379	411	99	437	Yes
HT	180	24	379	410	99	438	No
HT	180	24	380	411	99	438	Yes

<sup>a</sup>  $T$  = temperature;  $t$  = time; \*Raman modes = ( $\text{cm}^{-1}$ ); Ref. = reference; for all the syntheses performed in this study, the reaction time was 24 h; CTAB = presence of cetyl trimethylammonium bromide; CL = charged liquid cluster beam; ET = thermal evaporation; SG = sol-gel; CP = coprecipitation; HT = hydrothermal; MH = hydrothermal microwave; BK = bulk; TR = theoretical.

The samples analysed in this study also presented other signals that are not displayed in Fig. 4, such as a wide band of low intensity that appears right above 550  $\text{cm}^{-1}$ , which can be attributed to modes  $A_1$ (LO) and  $E_1$ (LO). The appearance of bands  $A_1$ (LO) and  $E_1$ (LO) in the Raman spectra of ZnO is caused by the formation of structural faults (oxygen and interstitial zinc vacancies), where mode  $E_1$ (LO) is more strongly affected by these effects.<sup>75</sup> The wide band, which also appeared in the Raman spectra with peaks approaching 1100 and 1150  $\text{cm}^{-1}$ , corresponds to 2LO (mode  $A_1$ ).<sup>5</sup> Zhao *et al.*<sup>76</sup> reported the possibility of locating a peak at approximately 1350  $\text{cm}^{-1}$ , which would indicate three phonons from the Raman scattering processes,  $A_1$ (TO) +  $A_1$ (LO) +  $E_2$ H; however, these peaks do not appear in the Raman spectra of this study.

The information in Table 3 indicates consonance between the Raman modes identified and attributed in this study and



other studies published in the literature, although there is a slight displacement in the relative position of some peaks. The small changes observed in the characteristic positions of the Raman modes listed in Table 3 can be associated with the degree of crystallinity, grain size distribution and average crystal size, ionic interaction force, degree of structural order and disorder in the crystal lattice, and the presence of structural defects (oxygen vacancy, distortions and/or tensions in the structure). These alterations are confirmed by the PL spectra. The visible band in the PL spectrum only appears in the presence of defects such as  $V_o$  of  $O_2$  and interstitial  $O_i$ , among others.<sup>77,78</sup> Special attention is given to the efficiency of the hydrothermal method used in this study, as the main characteristic Raman modes for the ZnO wurtzite phase were observed as well as peaks that were not exhibited in other studies in the literature, where less energetic and drastic reaction conditions were applied.

IR spectroscopy is a useful and powerful technique adopted for the analysis, confirmation and elucidation of structures of compounds and to identify the functional groups present in the compounds,<sup>79</sup> complementing the information obtained from Raman spectroscopy. IR analyses using KBr pellets in transmission mode are displayed in Fig. 5 for the samples hydrothermally processed for 24 h at 180 °C, with and without CTAB.

The IR spectra displayed absorption bands between 3400 and 2900  $cm^{-1}$ , which refer to O–H and C–H vibrations, respectively, where the O–H absorption most likely originates from the atmospheric mixture where the analyses are performed, which adsorbs on the surface of the samples and on the KBr pellets.<sup>80</sup> The modes close to 1400 and 1600  $cm^{-1}$  represent C=O asymmetrical and symmetrical stretching, respectively, and may be associated with the residue from the starting material,  $Zn(CH_3COO)_2 \cdot 2H_2O$ , still present in the final product.<sup>81</sup> Nevertheless, emphasis is given to the superposition of bands at approximately 500  $cm^{-1}$ , referent to the Zn–O stretching frequency, which is present in all the samples

analysed by IR and is indicative of the high orientation of the ZnO wurtzite crystal structure.<sup>79</sup>

The superposed bands located at approximately 420, 580 and 590  $cm^{-1}$  are attributed to modes  $E_1(TO)$ ,  $A_1(LO)$  and  $E_1(LO)$ , respectively.<sup>82</sup> Another characteristic band of the ZnO wurtzite phase should appear at approximately 380  $cm^{-1}$ , referent to mode  $A_1(TO)$ ; however, because of the limitations of the equipment used for the analyses, measurements below 400  $cm^{-1}$  could not be performed using KBr pellets in transmission mode.

### 3.4. FE-SEM analyses

The FE-SEM micrographs presented in Fig. 6(a–f) show the morphology of the ZnO microcrystals prepared at 120, 150 and 180 °C for 24 h, with and without CTAB. The FE-SEM micrographs demonstrate the predominance of ZnO microcrystals in the form of hexagonal columns in the absence of CTAB and of double hexagonal columns in the presence of CTAB. Similarly, for the samples synthesised at 180 °C in the presence or absence of CTAB, the shape of the hexagonal columns is different, as the (001) crystal face exhibits a smaller diameter in relation to face (00 $\bar{1}$ ). Hence, these ZnO samples synthesised at 180 °C were analysed using energy dispersive spectroscopy (EDS) to evaluate the chemical composition. The insert in Fig. 6(e and f) shows a typical EDS spectrum of ZnO crystals.<sup>16</sup> The result confirms that each crystal is composed of Zn and O (the Au and C peaks originate from elements in the sample holder).

Based on the FE-SEM images, the crystal size distribution was estimated considering the average of 100 particles ( $N = 100$ ) for every one of the synthesised samples in this study, as illustrated in Fig. 7. The size estimations were performed considering each particle individually, including those that exhibited the form of a double hexagonal column, as observed for the samples processed in the presence of CTAB.

The ZnO microcrystals exhibit a polydisperse particle size distribution. Fig. 7 shows the tendency of reduction in the average size of individual microcrystals with an increase in temperature from 95 to 97% (without CTAB) and from 74 to 77% (with CTAB). The reduction of the average size is more evident in the samples prepared at 180 °C. Additionally, the presence of CTAB affects the growth of the ZnO microcrystals, where, for the same processing conditions, the average size of individual microcrystals was between 46 and 93% larger.

Recently, different ZnO morphologies, such as rods, flowers, spheres, disks, and hexagonal columns, have been synthesised using different methods, as displayed in Table 4.<sup>2,5,11,16,27,46,68,83–96</sup> Various methods can be used to obtain ZnO crystal structures; however, the hydrothermal approach from aqueous solutions offers advantages, such as the low processing temperature and the use of simple material, its appropriateness for large-scale application and economic advantages.<sup>83</sup>

### 3.5. Growth process

Based on the experimental results and orientation type of crystal growth, the possible growth mechanism of ZnO crystals of hexagonal column form belongs to the Ostwald ripening mechanism and is also involved in the selective adsorption of

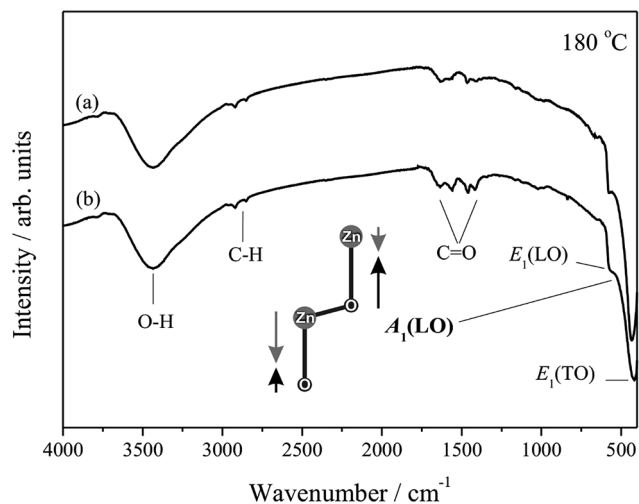


Fig. 5 Infrared spectra of samples of ZnO hydrothermally processed for 24 h at 180 °C in the absence (a) and presence (b) CTAB. The  $A_1$  mode(LO) is shown.



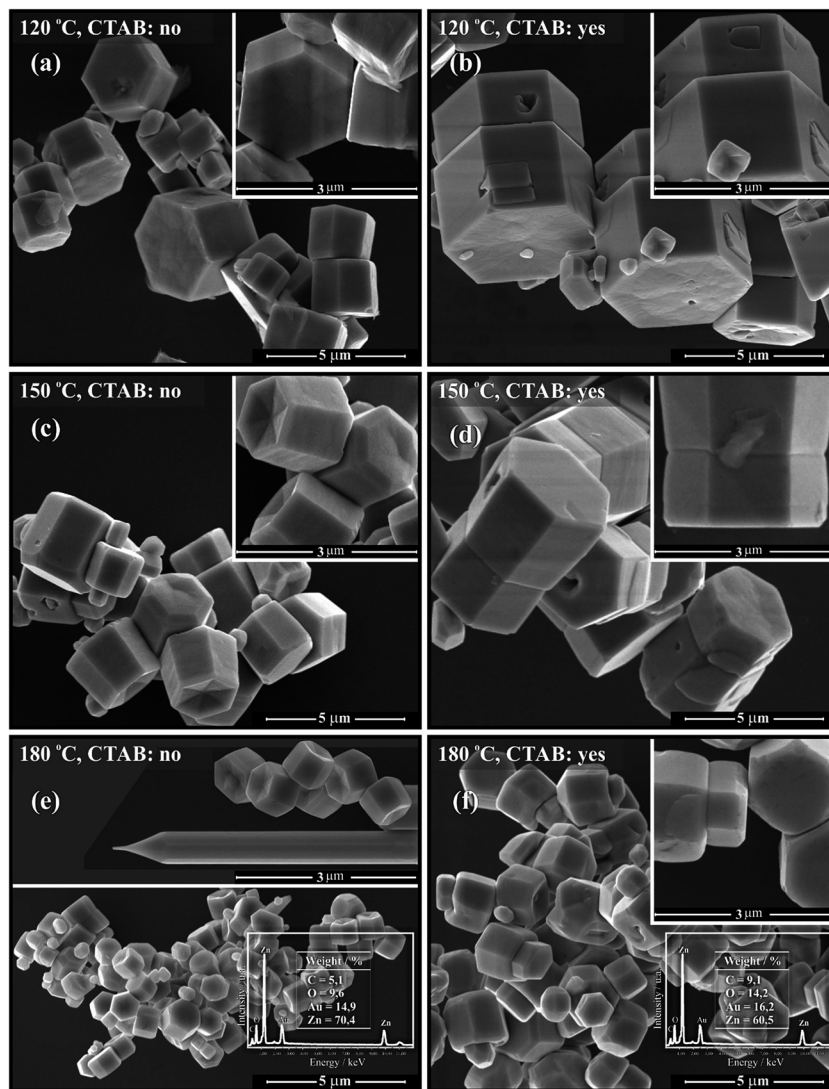
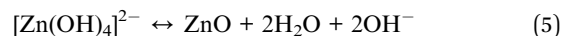
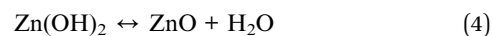
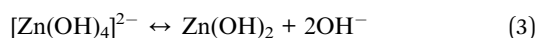


Fig. 6 FE-SEM micrographs of ZnO microstructures obtained by hydrothermal processing at 120 °C (a) without and (b) with the assistance of CTAB; at 150 °C (c) without and (d) the assistance of CTAB; and at 180 °C (e) without and (f) with the assistance of CTAB. The energy dispersive spectroscopy (EDS) elemental analysis is displayed as an insertion for the samples obtained at 180 °C (e and f).

zincate growth units  $[\text{Zn}(\text{OH})_4]^{2-}$  along the polar axis  $[001]$  of the ZnO crystal structure.<sup>92</sup> This process is considered simple and innovative.<sup>87</sup>

The crystal formation process includes nucleation and growth. Initially, because of the decomposition of ZAD at high temperature, the concentrations of  $\text{Zn}^{2+}$  and  $\text{OH}^-$  increase correspondingly. When the supersaturation degree exceeds the critical value, the ZnO nuclei start to form. The mechanism suggested in this study for the formation of ZnO microcrystals hydrothermally processed at 120, 150 and 180 °C, with and without the assistance of CTAB, is proposed in Fig. 8.

The ZnO synthesis without surfactant addition is classified as “organic-free”.<sup>88</sup> Under hydrothermal conditions, the possible involved reactions are



The experimental results revealed that the hydrothermal conditions, particularly the basic concentration of the solution and the temperature, affect the morphology and size of the crystallite. The modification of the physico-chemical conditions during the growth process is considered to essentially alter the solution structure, *i.e.*, the structural form of the growth units and the nature of the growth interfaces. Therefore, an approach could be performed in relation to the incorporation of growth units in the different faces and the nature of the crystal growth interfaces under the effect of the addition of  $\text{OH}^-$  ions to interpret the formation mechanism of the observed morphology.

The ZAD precursor undergoes hydrolysis, which induces the formation of  $\text{Zn}(\text{OH})_2$ . The  $\text{Zn}(\text{OH})_2$  is a hydroxide of



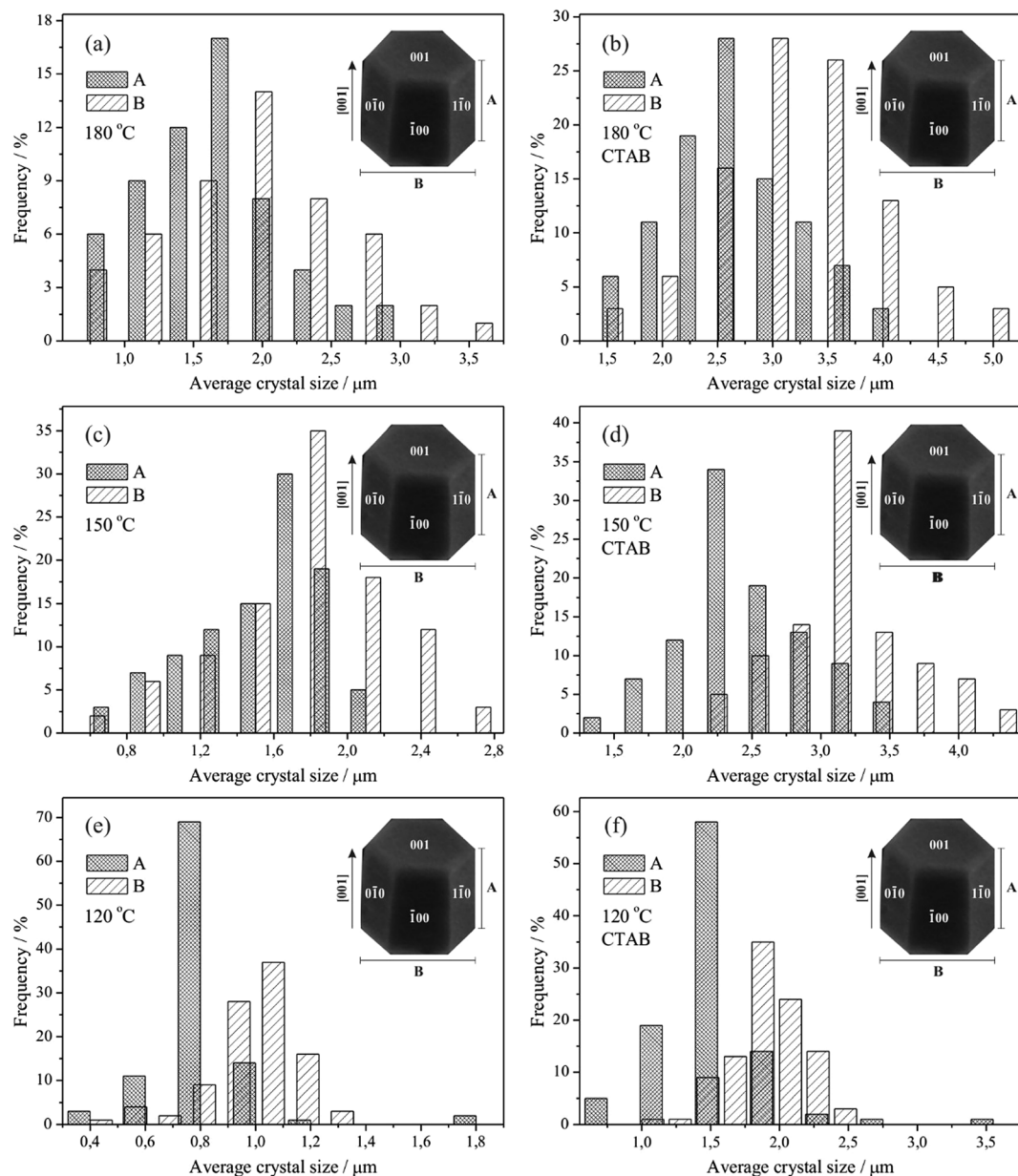


Fig. 7 Size distribution of ZnO microcrystals obtained by hydrothermal processing with  $N = 100$  at 120 °C (a) in the absence and (b) presence of CTAB; at 150 °C (c) in the absence and (d) presence of CTAB; and at 180 °C (e) in the absence and (f) presence of CTAB.

amphoteric character, and its solubility is particularly related to the alkalinity of the solution and the temperature.<sup>97</sup> Thus, the solubility increases with the increase of temperature.  $\text{Zn}(\text{OH})_2$  is dissolved in the solution to form the zincate complex  $[\text{Zn}(\text{OH})_4]^{2-}$  in the basic solution; these complex groups are called crystal growth units, where these growth units dehydrate when they are incorporated in the crystal.<sup>46</sup> Furthermore, the complexes (growth units) exhibit polaron behaviour because of the tetrahedron structure characteristic, *i.e.*, the asymmetrical position of the Zn atom. The vertex of the tetrahedral exhibits a negative charge, whereas the base exhibits a positive charge and, similarly, the structured units, *i.e.*, the  $\text{Zn}-\text{O}_4$  crystal tetrahedron. In turn, the amount of  $\text{OH}^-$  in the solution has

a significant effect on the nature of the growth interface, particularly on the two polar faces, and therefore on the rate of incorporation in these faces.

The detailed analyses of the incorporation of  $[\text{Zn}(\text{OH})_4]^{2-}$  (zincate) growth units on the positive and negative faces are described next. In a solution with high pH under hydrothermal conditions, the starting material is completely dissolved, and all that is dissolved in the form of  $\text{Zn}(\text{OH})_2$  is complexed with  $\text{OH}^-$  to form zincate  $[\text{Zn}(\text{OH})_4]^{2-}$ , which exhibits a negative charge. In turn, reminiscent  $\text{OH}^-$  remains in the solution, which can affect the growth interface. Once the positive crystal face (001) is occupied by Zn atoms, the  $\text{OH}^-$  ions in solution can be adsorbed on the face and modify the nature of the interface.<sup>16</sup>



**Table 4** Morphology and size of ZnO micro- and nanocrystal structures from studies reported in the literature, obtained using different synthesis methods<sup>a</sup>

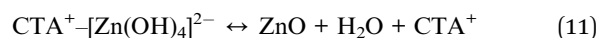
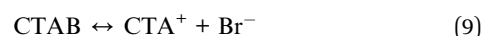
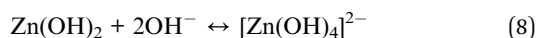
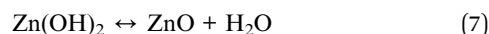
Reagents	M	T (°C)	t (h)	Form	Size (μm)	Ref.
Zn(NO <sub>3</sub> ) <sub>2</sub>	CC	500	0.08	Mushroom	60	84
Zn(CH <sub>3</sub> COO) <sub>2</sub> + ED	SG	500	2	Rod	1.5	85
ZnSO <sub>4</sub> + HMT + ED	TM	240	1	Flower	>1	86
Zn(NO <sub>3</sub> ) <sub>2</sub> + (NH <sub>4</sub> ) <sub>2</sub> CO <sub>3</sub> + CTAB + C <sub>2</sub> H <sub>6</sub> O	ST	220	18	Rod	0.8	45
Zn(CH <sub>3</sub> COO) <sub>2</sub> + NaOH + CTAB	HT	200	20	Rod	>20	87
Zn(CH <sub>3</sub> COO) <sub>2</sub> + NaOH	HT	200	20	Flower	>4	88
Zn(NO <sub>3</sub> ) <sub>2</sub> + CTAB	HT	200	10	Rod	1	16
Zn(CH <sub>3</sub> COO) <sub>2</sub> + KOH + CTAB	HT	180	24	Kale	3	89
Zinc powder + CTAB	HT	180	24	Rod	1	46
Zn(CH <sub>3</sub> COO) <sub>2</sub> + NaOH + CTAB	HT	180	20	Flower	4	90
Zn + (NH <sub>4</sub> ) <sub>2</sub> S <sub>2</sub> O <sub>8</sub> + KOH + CTAB	HT	160	15	Rod	10	91
Zn(CH <sub>3</sub> COO) <sub>2</sub> + CTAB + C <sub>6</sub> H <sub>12</sub> + C <sub>4</sub> H <sub>10</sub> O + (CH <sub>2</sub> ) <sub>6</sub> N <sub>4</sub>	ST	140	14	Dumbbell	8	92
ZnCl <sub>2</sub> + NaOH + CTAB	HT	130	24	Rod	>5	11
Zn(CH <sub>3</sub> COO) <sub>2</sub> + NaOH + CTAB	HM	130	3	Threads	>15	68
Zn(CH <sub>3</sub> COO) <sub>2</sub> + NaOH + PVP	HT	120	72	Sphere	0.04	5
ZnCl <sub>2</sub> + NaOH + SDS + IBA	HT	120	12	Disk	>5	2
Zn(CH <sub>3</sub> COO) <sub>2</sub> + KOH + CTAB	HT	120	5	Column	1.4	93
Zn(NO <sub>3</sub> ) <sub>2</sub> + NaOH + CTAB	HT	120	0.5	Sisal	6	94
Zn(NO <sub>3</sub> ) <sub>2</sub> + NH <sub>4</sub> OH	HT	100	10	Rotor	3	95
Zn(NO <sub>3</sub> ) <sub>2</sub> + U + EG	HT	90	0.5	Dumbbell	>0.5	96
Zn(NO <sub>3</sub> ) <sub>2</sub> + NH <sub>4</sub> OH + CTAB	CP	25	10	Leaf	1	27

<sup>a</sup> M = method; T = temperature; t = time; size = size; Ref. = reference; CC = calcination; SG = sol-gel; TM = thermolysis; ST = solvothermal; HT = hydrothermal; HM = hydrothermal microwave; CP = coprecipitation; Zn(NO<sub>3</sub>)<sub>2</sub> = zinc nitrate; Zn(CH<sub>3</sub>COO)<sub>2</sub> = zinc acetate; ED = ethylenediamine; HMT = hexamethylenetetramine; (NH<sub>4</sub>)<sub>2</sub>CO<sub>3</sub> = ammonium carbonate; CTAB = cetyl trimethylammonium bromide; C<sub>2</sub>H<sub>6</sub>O = ethanol; NaOH = sodium hydroxide; KOH = potassium hydroxide; Zn = zinc powder; (NH<sub>4</sub>)<sub>2</sub>S<sub>2</sub>O<sub>8</sub> = ammonium peroxodisulphate; C<sub>6</sub>H<sub>12</sub> = cyclohexane; C<sub>4</sub>H<sub>10</sub>O = *n*-butanol; (CH<sub>2</sub>)<sub>6</sub>N<sub>4</sub> = methenamine; ZnCl<sub>2</sub> = zinc chloride; PVP = polyvinylpyrrolidone; SDS = sodium dodecyl sulphate; IBA = isobutanol; NH<sub>4</sub>OH = ammonium hydroxide; U = urea; EG = ethylene glycol.

Therefore, it becomes more difficult to incorporate the growth units on the positive and negative faces. The polar faces grow slowly and are developed with larger size, resulting into a regular morphology, such as hexagonal columns. According to observations, the temperature accelerates the reaction process, and at 180 °C, the (001) face tends to be smaller in the final stage.

Wang *et al.*<sup>46</sup> reported that Zn(OH)<sub>2</sub> not only contributes to the nucleation of ZnO as previously mentioned but also transforms into zincate [Zn(OH)<sub>4</sub>]<sup>2-</sup>, increasing the growth rate of ZnO. Furthermore, in the reaction at high temperature, active sites can be generated around the circumference of the ZnO nucleus, causing the ZnO to grow preferentially in the active known to be a polar crystal whose positive plane is rich in Zn and whose negative plane is rich in O. In the hydrothermal process, the growth unit [Zn(OH)<sub>4</sub>]<sup>2-</sup> leads to different growth rates of the planes: V(001) > V(110) > V(100) > V(101) > V(001).<sup>88</sup> Generally, a faster growth rate corresponds to faster disappearance of the plane. Therefore, the (001) plane of ZnO, with a fast growth rate associated with the high temperature, tends to disappear at the end of the hydrothermal process, which generates the point at the end of the *c* axis. In turn, the (001) plane, the slower growth rate plane, is maintained during the hydrothermal process. Hence, at 180 °C, at higher temperature, the form of the hexagonal columns can be altered, with a thinner (001) crystal face.

A possible growth mechanism for the ZnO microstructures at different temperatures and in the presence of CTAB is described next. The following chemical reactions are involved in the process:



The presence of CTAB, which is a cationic surfactant, reduces the surface tension of the solution, which decreases the energy necessary to form a new phase, and therefore, the ZnO crystals can be formed at a temperature lower than supersaturation. As previously mentioned, the ZnO crystal growth unit is zincate [Zn(OH)<sub>4</sub>]<sup>2-</sup>; therefore, in aqueous solutions, the [Zn(OH)<sub>4</sub>]<sup>2-</sup> anions and CTA<sup>+</sup> cations in solution during the hydrothermal process interact electrostatically to form complexing agents that are adsorbed on the surface of ZnO nuclei. Because of this adsorption, the surface energy of the ZnO



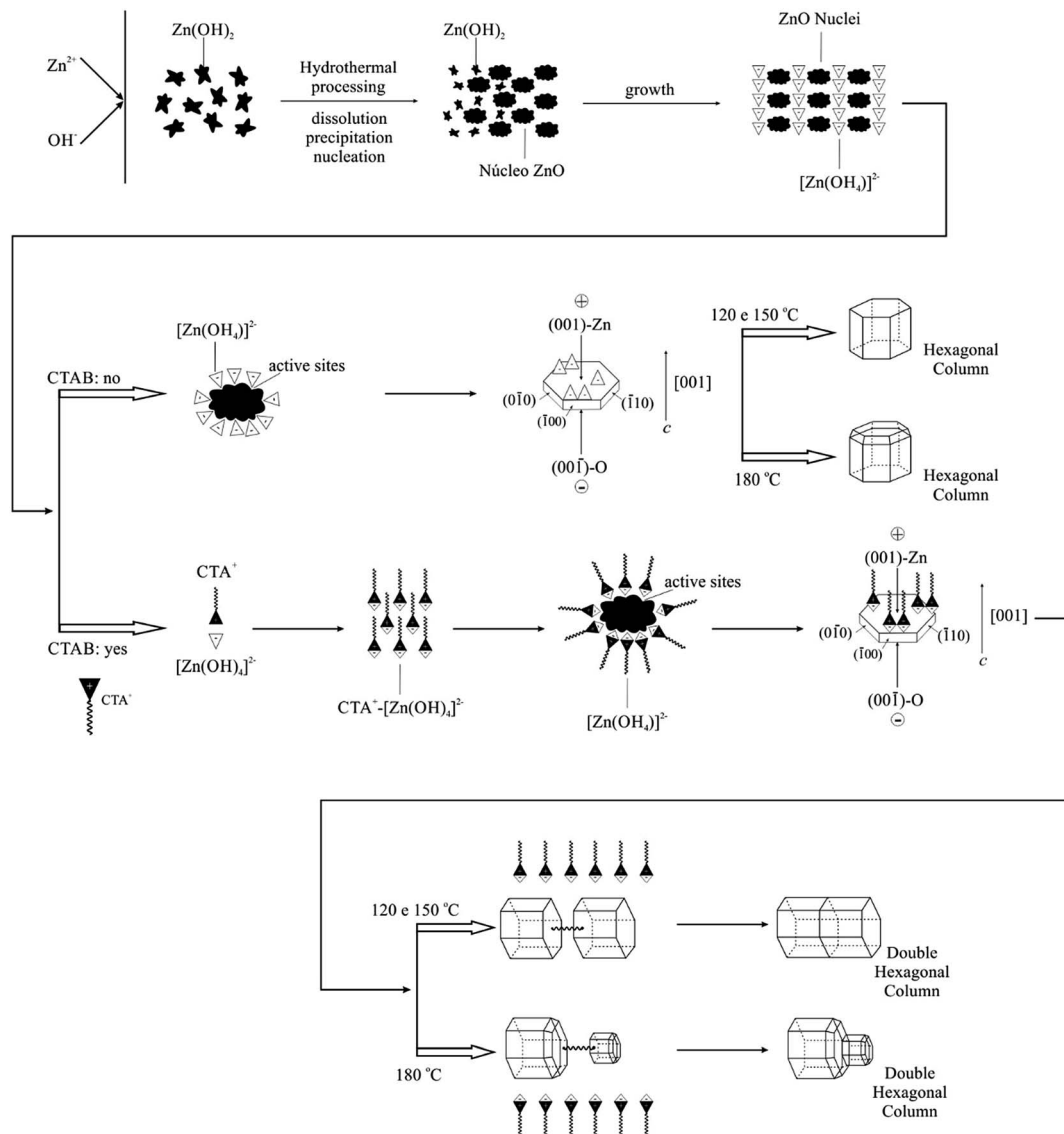


Fig. 8 Schematic diagram of the mechanism proposed for the growth of ZnO microstructures in the form of simple and double hexagonal columns, obtained by hydrothermal processing at 120, 150 and 180 °C, with and without the assistance of CTAB.

nucleus decreases, resulting in active sites generated on the surface. Additionally, the temperature acts directly on the permanent dipole of water and increases the kinetic behaviour of crystallisation by one or two orders of magnitude.<sup>68</sup>

During the hydrothermal process, the CTAB acts as a transportation mode for the  $[\text{Zn}(\text{OH})_4]^{2-}$  growth units. According to the internal structure and crystal growth cell, the ZnO exhibits a preferential growth behaviour along the  $c$  axis. These growth units are combined among themselves and decompose into ZnO nuclei simultaneously from the tetrahedral face of Zn–O<sub>4</sub> and auto-organise to form microstructures in the form of hexagonal columns. The number of  $[\text{Zn}(\text{OH})_4]^{2-}$  growth units increases at 180 °C, most likely because the high temperature accelerates the microcrystal growth reaction; consequently, the number of ZnO nuclei also decreases, reducing the surface potential.<sup>89</sup>

For hydrothermal processing with the assistance of CTAB, the same previously mentioned comments are valid. The ZnO microcrystal formation process under hydrothermal conditions can be represented as follows: the ZAD precursor undergoes hydrolysis, which induces the formation of  $\text{Zn}(\text{OH})_2$ . During the hydrothermal process, some of the  $\text{Zn}(\text{OH})_2$  colloids are dissolved into  $\text{Zn}^{2+}$  and  $\text{OH}^-$ . When the concentrations of  $\text{Zn}^{2+}$  and  $\text{OH}^-$  reach the ZnO supersaturation degree, the ZnO nucleus is formed. The  $[\text{Zn}(\text{OH})_4]^{2-}$  growth units exhibit a tetrahedral geometry.<sup>98–100</sup>

The CTAB is completely ionised in water. The  $\text{CTA}^+$  is positively charged with a tetrahedral head and a long hydrophobic tail. The resulting cation is also a tetrahedron with a long hydrophobic tail. Therefore, ion pairs can be formed between  $[\text{Zn}(\text{OH})_4]^{2-}$  and  $\text{CTA}^+$  because of the electrostatic interaction. The critical micelle concentration (CMC) of the pure CTAB in



aqueous solution at 25 °C is 0.0009 M,<sup>45</sup> and the CTAB concentration used in this study is approximately 0.1 M, and, in this case, the CTAB aggregation in aqueous solution forms spherical micelles. Only the micelles in aqueous solutions are in dynamic equilibrium; the  $[\text{Zn}(\text{OH})_4]^{2-}$  and  $\text{CTA}^+$  ion pairs are constantly adsorbed and separated at the surface of the formed micelle. The complementarity between  $[\text{Zn}(\text{OH})_4]^{2-}$  and  $\text{CTA}^+$  enables the surfactant to act as an ionic carrier. It should also be highlighted that the CMC of CTAB increases as the temperature increases.<sup>45</sup>

According to Sun *et al.*,<sup>46</sup> in the presence of CTAB, a fluctuating film is formed. When the surfactant agent molecules exit, zincate is transported in the form of an ionic pair, such that the boundary layer becomes finer, which facilitates the interaction process of the active sites. In the crystallisation process, the surfactant molecules can act as growth controllers as well as agglomeration inhibitors by forming a film on the newly formed ZnO crystal.

The adsorption of growth units at the crystal surface strongly affects the rate of formation and orientation of crystals. When a ZnO crystal grows, a surfactant film can be formed at the interface between the solution and ZnO crystal, reducing the interface energy. The floating film and surfactant molecules that transport the growth units will release them on the surface of the ZnO crystal. As the CTAB favours the formation of a film where the molecules tend to be perpendicular to the adsorbed surface, the growth units tend to fit in the face at the growth interface. Thus, this type of fit and the dehydration result in three Zn–O–Zn bonds, making this fit mode predominant and competing with others as the fitting in the vertex and edge. The ZnO crystal grows preferentially along the *c* axis ([001] direction) due to this fitting type in the (001) crystal face and the repeated dehydration steps. According to the previously mentioned process, it is supposed that CTAB not only accelerates the reaction as a growth unit transporter but also leads to the oriented growth of the ZnO microcrystals.<sup>27</sup>

Liu *et al.*<sup>92</sup> reported that in the initial hydrothermal process, the growth unit of negative nature  $[\text{Zn}(\text{OH})_4]^{2-}$  leads to different growth rates of ZnO particle planes and lamellas, which will be easily developed because of the Ostwald ripening process.<sup>96</sup> As the reaction occurs, initially, the large surface areas of the lamellar crystals are dissolved and re-precipitate to form larger crystals of low energy and hexagonal morphology of double hexagonal columns. Recent studies with similar morphologies identified defects at the basal plane with inversion domain boundaries (IDBs). When the boundary inversion is formed in the ZnO, the head-to-head configuration appears predominantly along the polar axis *c*, *i.e.*, planes with oxygen terminations oriented towards the other plane interface (001). In fact, the formation of double microstructures involves structural and energetic factors; however, the driving force behind the formation of this type of morphology remains under discussion in the literature.<sup>92</sup> Gao *et al.*<sup>86</sup> believe that the formation of double crystals in ZnO samples prepared under hydrothermal conditions is linked to the presence of organic additives, which provide models for the nucleation and orientation of ZnO crystal growth and, consequently, results in units in the form of fuse (axis), with half of the interface. Wang *et al.*<sup>101</sup> reported the synthesis of ZnO in the form

of dumbbells (double crystal) by the hydrothermal process using  $\text{K}^+$  as a mineraliser. In this hydrothermally process,  $\text{K}^+$  can act as a bond unit between tetrahedral  $[\text{ZnO}_4]^{6-}$  and leads to the initial formation of a double crystal nucleus, with head-to-head or tetrahedral tail-to-tail orientation depending on the conditions of preparation. In turn, in the present study, the majority of  $\text{Zn}^{2+}$  ions were precipitated as  $\text{Zn}(\text{OH})_2$ . Under hydrothermal conditions, the  $\text{Zn}(\text{OH})_2$  precipitates were transformed into  $[\text{Zn}(\text{OH})_4]^{2-}$  growth units. In the presence of CTAB, the growth units can be bonded by CTAB in the (001) composition plane to form the crystal nuclei in the form of double hexagonal columns. To reduce the surface energy, the individual crystallite growth in the double crystal occurs along the *c* polar axis by incorporating units in the (001) growth interfaces, and therefore, ZnO crystals in the form of double hexagonal columns are ultimately formed.

### 3.6. Diffuse reflectance

The direct optical band gap energy ( $E_g$ ) was calculated using the method proposed by Kubelka and Munk.<sup>102</sup> This methodology is based on the transformation of the diffuse reflectance measurements ( $R$ ) to estimate the optical  $E_g$  values with good precision. The equation by Kubelka–Munk (12) for any wavelength is described as

$$F(R_\infty) = \frac{(1 - R_\infty)^2}{2R_\infty} = \frac{k}{s} \quad (12)$$

The analyses were performed using magnesium oxide ( $\text{MgO}$ ) as the reference standard, where  $R_\infty = R_{\text{sample}}/R_{\text{MgO}}$  ( $R_\infty$  is the reflectance when the sample has infinite thickness),  $k$  is the coefficient of molar absorption and  $s$  is the scattering coefficient. In a parabolic band structure, the optical  $E_g$  and absorption coefficient of semiconducting oxides can be calculated using eqn (13):

$$\alpha h\nu = C_1(h\nu - E_g)^n \quad (13)$$

where  $\alpha$  is the coefficient of linear absorption of the material,  $h\nu$  is the photon energy,  $C_1$  is the proportionality constant,  $E_g$  is the optical band gap and  $n$  is the constant associated with different types of electronic transitions ( $n = 0.5$ , direct allowed;  $n = 2$ , indirect allowed;  $n = 1.5$ , indirect forbidden; and  $n = 3$ , direct forbidden). According to the literature, wurtzite ZnO exhibits an optical absorption spectrum ruled by direct electronic transitions.<sup>5</sup> In this phenomenon, after the electronic absorption process, the electrons located in the maximum energy states in the valence shell return to the minimum energy states in the conduction band under the same point of the Brillouin zone. Based on this information, the  $E_g$  values of ZnO were calculated using  $n = 0.5$  in eqn (13). Finally, using the remission function and the  $k = 2\alpha$  term, the modified Kubelka–Munk equation was obtained, as shown in eqn (14):

$$[F(R_\infty)h\nu]^2 = C_2(h\nu - E_g) \quad (14)$$

Consequently, after determining the value of  $F(R_\infty)$  from eqn (14) and plotting a graph of  $[F(R_\infty)h\nu]^2$  versus  $h\nu$  and  $C_2$ , the  $E_g$  of



the ZnO crystals was determined by extrapolation of the linear region of the curves, making  $[F(R)h\nu]^2 = 0$ , as shown in Fig. 9.

Fig. 9 shows that the optical  $E_g$  values of ZnO crystals hydrothermally synthesised without CTAB varied from 3.15 to 3.20 eV, and those synthesised with CTAB varied from 3.13 to 3.21 eV. In this case, it was verified that the optical  $E_g$  values increase with decreasing particle size and increasing temperature for the samples synthesised with or without CTAB, which may suggest that ZnO crystals prepared at 120 and 150 °C absorb more visible light and that at 180 °C, this absorption is smaller.<sup>5</sup>

Table 5 presents the experimental values of optical  $E_g$  for ZnO crystals reported in the literature, which were obtained using different synthesis and bulk methods. The optical  $E_g$

values for the ZnO crystals (Fig. 9) differ slightly from the values reported in the literature for pure ZnO crystals. These discrepancies can be attributed to the fact that optical  $E_g$  is strongly dependent on the synthesis method, defect levels in the optical band gap, morphology and average crystal size, structural orientation and distortions.<sup>103</sup> Next, some considerations are made regarding these effects.<sup>79,103–110</sup>

As previously stated,  $E_g$  can be affected by various factors, including crystal defects<sup>111–113</sup> and sizes.<sup>114,115</sup> Huo and Hu<sup>104</sup> demonstrated a linear correlation between the  $E_g$  of ZnO and the size of the crystal nanoparticles, which indicates that the increase of  $E_g$  can be attributed to the decrease of the crystal size. It is also known that when the crystal size is very small (nanometric scale),  $E_g$  increases as the crystal size

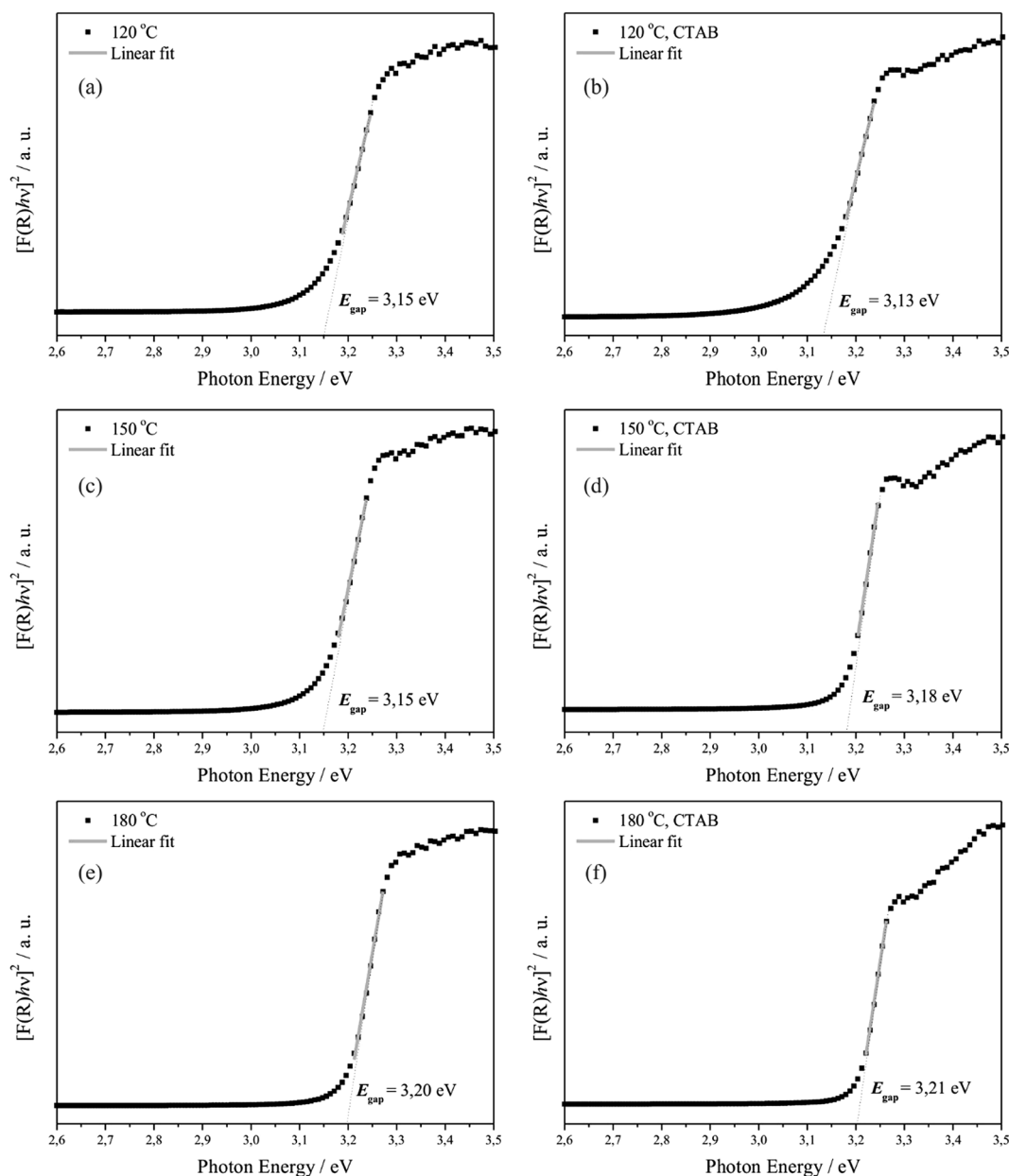


Fig. 9 Kubelka–Munk curves ( $[F(R)h\nu]^2$  versus  $h\nu$  in eV) of the ZnO samples hydrothermally processed for 24 h at 120 °C (a) without and (b) with the assistance of CTAB; at 150 °C (c) without and (d) with the assistance of CTAB; and at 180 °C (e) without and (f) with the assistance of CTAB.



**Table 5** Experimental values of the band gap energy ( $E_g$ ) of ZnO crystals reported in the literature obtained using different synthesis and bulk methods<sup>a</sup>

	$T$ (°C)	$t$ (h)	$E_g$ (eV)	Ref.
<b>Synthesis methods</b>				
CC	1000	4	3.12	87
PC	700	1	3.25	105
PT	600	1	3.17	106
GR	600	1	3.14	103
SG	400	1	3.20	107
PM	200	2	3.26	79
HT	90	6	3.36	108
<b>Bulks</b>				
BK	—	—	3.35	109
BK	—	—	3.36	110

<sup>a</sup> M = method;  $T$  = temperature;  $t$  = time;  $E_g$  = band gap; Ref. = reference; CC = calcination; PC = Pechini; PT = precipitation; GR = grinding; SG = sol-gel; PM = precipitation and microwave; HT = hydrothermal; BK = bulk.

decreases.<sup>116,117</sup> However, the dependence of  $E_g$  on size has not yet been reported for crystal particles larger than 100 nm.<sup>104</sup> The results of this study demonstrate that the dependence of  $E_g$  in relation to size occurs even at the micrometric scale.

Considering the molecular orbitals, two factors can determine the changes of  $E_g$  with the increase of crystal size: the Coulomb interaction displaces  $E_g$  to lower values, whereas the quantum location displaces  $E_g$  to higher energies.<sup>105,118</sup> Hence, the apparent  $E_g$  tends to increase for a small crystal size, where the change in  $E_g$  is determined especially for the quantum location. In effect, the dependency of  $E_g$  with size is demonstrated in the literature for ZnO nanoparticles.<sup>116,117</sup> In contrast, when the crystal size is large,  $E_g$  tends to decrease because the Coulomb interaction plays a critical role in the change of  $E_g$  for crystals of larger sizes, which can explain the dependency of size on the  $E_g$  of large particles (>100 nm), which is the case in the present study.

### 3.7. PL emission

The PL property has always drawn attention from the scientific community, especially for the discovery of PL at room temperature, which favours its technological applications such as in LEDs, lasers in the visible light region and fibre optic components.<sup>119</sup>

The literature presents various models that explain this optical property, and among them, there is consensus that structural disorder is responsible for PL emission. A completely ordered or disordered material does not exhibit PL. Hence, a minimum order is necessary in a disordered system for the material to exhibit PL.<sup>120</sup>

All the synthesised samples (figure not shown) exhibit very similar band profiles and positions in the non-standardised PL emission spectra. One emission band is observed in the violet range, located at approximately 400 nm, with a small peak in the UV range approaching 380 nm, and intense and highly superposed emission bands that range from 440 to 750 nm (blue to red emission), with a maximum at approximately 610 nm.

PL is associated with the presence of structural disorder and is responsible for the formation of electronic levels within the band gap, *i.e.*, the formation of energy levels between the valence band (VB) and conduction band (CB). The energy levels between the VB and CB can act as recombination centres for the electron-gap pair, promoting luminescence emission. Generally, ZnO crystals with the wurtzite structure of macroscopic dimensions (bulk) and crystal organisation approaching the ideal exhibit strong UV emission, whereas smaller crystals (micro and nanostructures) associated with the abundance of defects exhibit strong emissions in the visible region, where the modifications at the ZnO structure surface can increase or suppress the intensity and emission in the visible range.<sup>116</sup>

The ratio of UV and visible emission intensities can be used to evaluate the quality of ZnO.<sup>121</sup> Generally, it is accepted that smaller ZnO crystal sizes are associated with PL emissions of low UV band ratios in relation to the visible band, caused by the large surface area and more surface defects.<sup>122</sup> However, this tendency was not verified in the present study. Possibly, there is the formation of steps with crystal side surfaces larger than ZnO, which may increase the surface/interface defects. Additionally, Zhou *et al.* (2002) suggest that for ZnO, intense emission bands in the visible range, more precisely above 500 nm, can be attributed to the presence of Zn(OH)<sub>2</sub> or OH<sup>-</sup> groups at the crystal surface level, which could also play the role of interstitial oxygen (O<sub>i</sub>). In other words, the excess of oxygen could lead to an increase of the number of defects in the crystal structure, elevating the intensity of the bands in the visible region. For the present study, where hydrothermal processing in alkaline pH is applied, this explanation is plausible for the observation of intense bands in the visible range, where hydroxyl groups or water at the surface can easily be present.<sup>123</sup> This explanation would not necessarily be applicable to ZnO samples produced by other methods. Hence, the presence of the emission band in the visible region of the PL spectra for the samples produced in this study corroborates the Raman results. In the Raman spectra, a slight variation was observed in the characteristic positions of the vibration modes that could be related to a series of factors including the crystallinity degree, grain size distribution and average crystal size, ionic interaction force, degree of structural order and disorder in the crystal lattice, and presence of structural defects (oxygen vacancies, distortions or tensions in the structure). Thus, the size distribution in all the samples had a direct effect on the intensity of the emission bands and not on its appearance. This type of study involving the variation of the particle size and intensity of the emission band in the visible region of the PL spectrum has already been reported for ZnO samples on the micrometric scale synthesised at hydrothermal conditions in the absence of CTAB.<sup>124</sup> The variations of the positions observed in the Raman modes and the appearance of the emission band in the PL spectra are observed in this study, which is intimately related to the presence of defects created during the sample processing. Although there are many studies in the literature on the types of defects that cause such effects on different types of materials, a more detailed investigation is necessary to properly correlate the defect type and effect that are susceptible to the preparation



conditions. Further studies are being performed to evaluate whether the defects in the samples produced in this study could be related to the presence of the  $\text{Zn}(\text{OH})_2$  species or whether  $\text{OH}^-$  groups could take the role of interstitial oxygen or whether the excess of oxygen in the reaction medium could be responsible for these changes of the ZnO characteristics.

### 3.8. Catalytic activity

Fig. 10 shows the photocatalytic activities of all samples for the degradation of RhB and MO aqueous solution under the simulative sunlight irradiation. The photocatalytic degradation of RhB as a function of time (Fig. 10a) was controlled of the ZnO samples obtained at different temperatures in the presence and absence of CTBA. The photolysis efficiency in absence of ZnO was less than 10% with irradiation for 90 minutes. The decolorization efficiencies of RhB degradation were 97%, 92% and 96% to ZnO obtained at 120, 150 and 180 °C in absence of CTBA, and 97%, 80% and 82% to ZnO obtained at 120, 150 and 180 °C with CTBA. Comparing to ZnO obtained without CTBA with ZnO obtained in presence of CTBA, it showed the RhB decolorization of 97%. Thus, the photocatalytic performance of the ZnO obtained at 120 °C in absence of CTAB is the highest, decolorizing RhB at 40 minutes.

The photocatalytic degradation of MO as a function of time (Fig. 10b) was controlled of the ZnO samples obtained at

different temperatures in the presence or absence of CTBA. The photolysis efficiency in absence of ZnO was less than 5% with irradiation for 90 minutes. The decolorization efficiencies of MB degradation were 99%, 63% and 82% to ZnO obtained at 120, 150 and 180 °C in absence of CTBA, and 81%, 58% and 65% to ZnO obtained at 120, 150 and 180 °C with CTBA. Comparing to ZnO obtained without and with CTBA, it is showed the MO decolorization of 99%. Thus, the photocatalytic performance of the ZnO obtained at 120 °C in presence of CTAB is the highest, decolorizing MO at 50 minutes.

The rate constant  $k$  (Fig. 10c and d) can be calculated by the gradient of  $\ln C_t/C_0 = f(t)$  because the degradation follows a pseudo-first order kinetics. The  $k$  value without catalyst equals  $1.33 \times 10^{-3} \text{ min}^{-1}$  and  $0.51 \times 10^{-3} \text{ min}^{-1}$  for degradation of RhB and MO, respectively. ZnO obtained without CTAB have  $k$  values of  $73.68 \times 10^{-3}$  (RhB degradation) and  $85.16 \times 10^{-3}$  (MO degradation), using ZnO obtained at 120 °C (Z120, Fig. 10) as catalysts (Fig. 10c and d). Degradation with as little as 100 mg of ZnO is more than 55 (RhB degradation) and more than 167 (MO degradation) times faster as without a catalyst. Compared to ZnO obtained in presence of CTAB, the catalyst obtained in absence (Zn120) are 2.0 times more efficient for degradation of RhB, and 4.8 times more efficient for degradation of MO. From the kinetic analysis, it has been established that the degradation of RhB and MO follows first order kinetics with trends

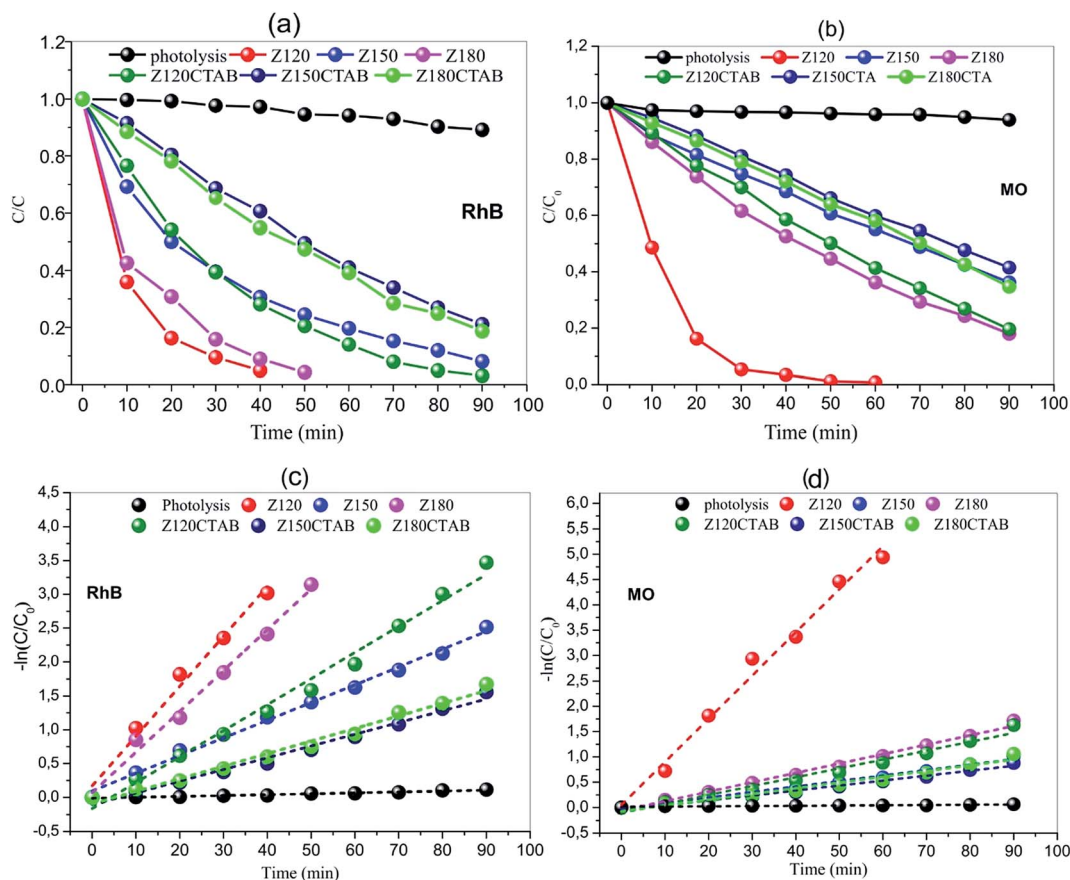


Fig. 10 Photocatalytic degradation of RhB and MO ((a) and (b), respectively) and kinetic data fitting for the degradation of RhB and MO ((c) and (d), respectively), using ZnO as catalyst.



Table 6 Rate constants of pseudo-first order ( $k$ ) and half-life time ( $t_{1/2}$ ) for RhB and MO degradation with ZnO as catalyst

Sample	RhB		MO	
	$k_{\text{ap}} \times 10^{-3} \text{ (min}^{-1}\text{)}$	$t_{1/2} \text{ (min)}$	$k_{\text{ap}} \times 10^{-3} \text{ (min}^{-1}\text{)}$	$t_{1/2} \text{ (min)}$
Photolysis	1.33	521.16	0.511	1356.4
Z120	73.68	9.40	85.16	8.1393
Z150	26.19	26.46	10.84	63.943
Z180	60.19	11.51	18.57	37.326
Z120CTAB	38.43	18.03	17.53	39.547
Z150CTAB	17.37	39.90	9.796	70.806
Z180CTAB	18.62	37.22	11.35	61.078

being displayed in Fig. 10 and the obtained values of kinetic rate constants given in Table 6.

Intensive research work is being undertaken globally to effectively use the process of photocatalysis for the degradation of organic pollutants from industrial effluents. Many photocatalysts such as  $\text{TiO}_2$ ,  $\text{MoO}_3$ ,  $\text{SnO}_2$ ,  $\text{WO}_3$ ,  $\text{Fe}_2\text{O}_3$ ,  $\text{Fe}_3\text{O}_4$ ,  $\text{Ag}_2\text{WO}_4$ ,  $\text{Ag}_2\text{MO}_4$ , etc. and combinations thereof, have been extensively investigated as suitable materials for pollutant degradation under UV/visible/solar light.<sup>125–133</sup> In general, several authors clearly show that morphology, and principally, both a high degree of crystallinity and moderate surface area are necessary to obtain highly active materials for organic pollutants degradation. The results obtained in this work are in good agreement with previous reports.<sup>134–136</sup> ZnO formed by the hydrothermal method exhibit high catalytic activity (Fig. 10).

## 4. Conclusion

The present study demonstrated that ZnO microcrystals with narrow size distributions can be successfully synthesised with chemical reproducibility in the wurtzite phase with the form of hexagonal columns starting from zinc acetate in alkaline medium at 120, 150 and 180 °C with and without the assistance of CTAB. The developed method is simple, allows for the production of ZnO microstructures in just 24 h of processing and uses common low-cost experimental apparatus, which is promising for industrial-scale application. Furthermore, the method offers control of the structural properties of the ZnO microcrystals by the appropriate selection of the reaction temperature, pH and the presence or absence of CTAB. These variables allow differentiated ZnO microcrystals to be prepared to meet the requirements of different technological applications. Photocatalytic degradation under UV irradiation reduced effectively the RhB and MO, with the best degradation results obtained for ZnO obtained at 120 °C and absence of CTAB. The differential of this work is the ZnO obtained from hydrothermal method, which can be easily separated from the solution using a simple filtration system with common filter paper, thus contributing to sustainable development and economically viable for industrial application, maintaining the high photocatalytic activity.

## Acknowledgements

The authors would like to acknowledge the support provided by the Federal University of Piauí (Universidade Federal do Piauí –

UFPI), the Laboratory of Nanocharacterisation of the Federal University of São Carlos (Universidade Federal de São Carlos – UFSCar), the São Paulo Research Foundation (Fundação de Amparo à Pesquisa do Estado de São Paulo – FAPESP) 2012/19926-8, the National Council for Scientific and Technological Development (Conselho Nacional de Desenvolvimento Científico e Tecnológico – CNPq) 473669/2012-9 and the Northeast Centre for Strategic Technologies (Centro de Tecnologias Estratégicas do Nordeste – CETENE).

## References

- Z. L. Wang, *J. Phys.: Condens. Matter*, 2004, **16**, R829–R858.
- K. Choi, T. Kang and S. G. Oh, *Mater. Lett.*, 2012, **75**, 240–243.
- Y. Masuda, N. Kinoshita, F. Sato and K. Koumoto, *Cryst. Growth Des.*, 2006, **6**, 75–78.
- P. F. Garcia, R. S. Mclean and M. H. Reilly, *Appl. Phys. Lett.*, 2006, **88**, 1235091–1235093.
- A. Stankovic, Z. Stojanovic, L. Veselinovic, S. D. Skapin, I. Bracko, S. Markovic and D. Uskokovic, *Mater. Sci. Eng., B*, 2012, **177**, 1038–1104.
- S. Baruah and J. Dutta, *Sci. Technol. Adv. Mater.*, 2009, **10**, 013001.
- R. Zhang, S. Kumar, S. Zou and L. L. Kerr, *Cryst. Growth Des.*, 2008, **8**, 381–383.
- X. Zhao, W. Liu, R. Chen, Y. Gao, B. Zhu, H. V. Demir, S. Wang and H. Sun, *Nanoscale*, 2016, **8**(11), 5835–5841.
- X. Zhang, S. Yang, S. Bi, A. Kumaresan, J. Zhou, J. Seifter, H. Mi, Y. Xu, Y. Zhang and H. Zhou, *RSC Adv.*, 2017, **7**, 12400–12406.
- W. L. Suchanek, *J. Cryst. Growth*, 2009, **312**, 100–108.
- Y. Yang, G. Du, X. Xin and B. Xu, *Appl. Phys. A*, 2011, **104**, 1229–1235.
- S. Ekambaram, *J. Alloys Compd.*, 2005, **390**, L4–L6.
- K. Byrappa, A. K. Subramani, S. Ananda, K. M. L. Rai, R. Dinesh and M. Yoshimura, *Bull. Mater. Sci.*, 2006, **29**, 433–438.
- Y. Sun, L. Chen, Y. Bao, Y. Zhang, J. Wang, M. Fu, J. Wu and D. Ye, *Catalysts*, 2016, **6**(12), 18891–18944.
- K. Schilling, B. Bradford, D. Castelli, E. Dufour, J. F. Nash, W. Pape, S. Schulte, I. Tooley, J. V. D. Boschi and F. Schellauf, *Photochem. Photobiol. Sci.*, 2010, **9**, 495–509.
- P. Rai, S. K. Tripathy, N. H. Park, O. Kwang-Joong, I. H. Lee and Y. T. Yu, *J. Mater. Sci.: Mater. Electron.*, 2009, **20**, 967–971.



- 17 A. Ammala, A. J. Hill, P. Meakin, S. J. Pas and T. W. J. Turney, *J. Nanopart. Res.*, 2002, **4**, 167–174.
- 18 M. H. Lai, A. Tubtimtae, M. W. Lee and G. J. Wang, *Int. J. Photoenergy*, 2010, 497095.
- 19 A. K. Barui, V. Veeriah, S. Mukherjee, J. Manna, A. K. Patel, S. Patra, K. Pal, S. Murali, R. K. Rana, S. Chatterjee and C. R. Patra, *Nanoscale*, 2012, **4**, 7861–7869.
- 20 I. M. M. Paino, F. J. Gonçalves, F. L. Souza and V. Zucolotto, *ACS Appl. Mater. Interfaces*, 2016, **8**, 32699–32705.
- 21 A. Moezzi, A. M. McDonagh and M. B. Cortie, *Chem. Eng. J.*, 2012, **185–186**, 1–22.
- 22 S. Bhushan, ed. D. R. Vij and N. Singh, *Materials Letters*, Zinc oxide Nova Science Publishers Inc., Commack Ny, 1998.
- 23 M. J. Height, L. Madler, S. E. Pratsinis and F. Krumeich, *Chem. Mater.*, 2006, **18**, 572–578.
- 24 M. A. Tshabalala, B. F. Dejene and H. C. Swart, *Physica B*, 2012, **407**, 1668–1671.
- 25 Y. W. Chen, Q. Qiao, Y. C. Liu and G. L. Yang, *J. Phys. Chem. C*, 2009, **113**, 7497–7502.
- 26 S. Music, D. Dragcevic and S. Popovic, *Mater. Lett.*, 2005, **59**, 2388–2393.
- 27 H. Tang, J. C. Chang, Y. Shan and S. T. Lee, *J. Phys. Chem. B*, 2008, **112**, 4016–4021.
- 28 M. Yoshimura and K. Byrappa, *J. Mater. Sci.*, 2008, **43**, 2085–2103.
- 29 K. Byrappa and T. Adschiri, *Prog. Cryst. Growth Charact. Mater.*, 2007, **53**, 117–166.
- 30 N. Tiwale, *Sens. Actuators, B*, 2014, **204**, 250–272; D. Ju, H. Xu, J. Zhang, J. Guo and B. Cao, *Sens. Actuators, B*, 2014, **201**, 444–451.
- 31 N. Tiwale, *Mater. Sci. Technol.*, 2015, **31(14)**, 1681–1697.
- 32 K. F. Cai, X. R. He and L. C. Zhang, *Mater. Lett.*, 2008, **62**, 1223–1225.
- 33 J. Zhan, H. Dong, Y. Liu, Y. Wang, Z. Chen and L. Zhang, *CrystEngComm*, 2013, **15**, 10272–10277.
- 34 J. Wang, R. Chen, Y. Xia, G. Wang, H. Zhao, L. Xiang and S. Komarneni, *Ceram. Int.*, 2017, **43**, 1870–1879.
- 35 K. N. Abbas and N. Bidin, *Appl. Surf. Sci.*, 2017, **394**, 498–508.
- 36 X. Zheng, R. Wu and Y. Chen, *Environ. Sci. Technol.*, 2011, **45**, 2826–2832.
- 37 N.-Q. Puay, G. Qiu and Y.-P. Ting, *J. Cleaner Prod.*, 2015, **88**, 139–145.
- 38 J. Choi, S. Chan, H. Joo, H. Yang and F. K. Ko, *Water Res.*, 2016, **101**, 362–369.
- 39 B. G. Wang, E. W. Shi and W. Z. Zhong, *Cryst. Res. Technol.*, 1998, **33**, 937–941.
- 40 C. Y. Toe, H. L. Tan, C. Boyer, A. Rawal, S. C. Thickett, J. Scott, R. Amal and Y. H. Ng, *J. Mater. Chem. A*, 2017, **5**, 4568–4575.
- 41 Y. Liu, X. Yan, Z. Kang, Y. Li, Y. Shen, Y. Sun, L. Wang and Y. Zhang, *Sci. Rep.*, 2016, **6**, 1–7.
- 42 J. S. Souza, W. M. Carvalho, F. L. Souza, C. Ponce-de-Leon, D. V. Bavykin and W. A. Alves, *J. Mater. Chem. A*, 2016, **4**, 944–952.
- 43 S. Adhikari, D. Sarkar and G. Madras, *RSC Adv.*, 2014, **4**, 55807–55814.
- 44 Y. Fang, Z. Li, S. Xu, D. Han and D. Lu, *J. Alloys Compd.*, 2013, **575**, 359–363.
- 45 L. Wolski, J. E. Whitten, I. Sobczak and M. Ziolek, *Mater. Res. Bull.*, 2017, **85**, 35–46.
- 46 Y. X. Wang, J. Sun, X. A. Fan and X. Yu, *Ceram. Int.*, 2011, **37**, 3431–3436.
- 47 H. Kato, K. Miyamoto and M. Sano, *Appl. Phys. Lett.*, 2004, **4**, 4562–4564.
- 48 M. Anbuvarannan, M. Ramesh, G. Viruthagiri, N. Shanmugam and N. Kannadasan, *Spectrochim. Acta, Part A*, 2015, **143**, 304–308.
- 49 H. Schulz and K. H. Thiemann, *Solid State Commun.*, 1979, **32**, 783–785.
- 50 <http://www.portaldapesquisa.com.br>, accessed in 11-06-2016.
- 51 Y. Chen, R. Yu, Q. Shi, J. Qina and F. Zheng, *Mater. Lett.*, 2007, **61**, 4438–4441.
- 52 G. Sun, M. Cao, Y. Wang, C. Hu, Y. Liu, L. Ren and Z. Pu, *Mater. Lett.*, 2006, **60**, 2777–2782.
- 53 C. Jiang, W. Zhang, G. Zou, W. Yu and Y. Qian, *J. Phys. Chem. B*, 2005, **109**, 1361–1361.
- 54 Y. H. Ni, X. W. Wei, J. M. Hong and Y. Ye, *Mater. Sci. Eng., B*, 2005, **121**, 42–47.
- 55 A. P. A. Oliveira, J. F. Hochepped, F. Grillon and M. H. Berger, *Chem. Mater.*, 2003, **15**, 3202–3207.
- 56 S. C. Abrahams and J. L. Bernstein, *Acta Crystallogr., Sect. B: Struct. Sci.*, 1969, **25**, 1233–1236.
- 57 K. Kiharai and G. Donnay, *Can. Mineral.*, 1985, **23**, 647–654.
- 58 L. B. Mccusker, R. B. V. Dreele, D. E. Cox, D. Louër and P. Scardi, *J. Appl. Crystallogr.*, 1999, **32**, 36–50.
- 59 J. M. A. Almeida, C. T. Menezes, A. S. Menezes, R. F. Jardim and J. M. Sasaki, *Magn. Magn. Mater.*, 2008, **320**, 304–307.
- 60 R. A. Young, *The Rietveld Method*, Oxford University Press, New York, 1995.
- 61 <http://www.crystalimpact.com/diamond>, accessed in 13-09-2016.
- 62 Ü. Özgür, Y. I. Alivov, C. Liu, A. Tekeb, M. A. Reshchikov, S. Doğan, V. Avrutin, S.-J. Cho and H. Morkoç, *J. Appl. Phys.*, 2005, **98**, 041301.
- 63 M. Koyano, P. Quocbao, L. T. Thanhbinh, L. Hongha, N. Ngoclong and S. Katayama, *Phys. Status Solidi A*, 2002, **193**, 125–131.
- 64 K. Mcguire, Z. W. Pan, Z. L. Wang, D. Milkie, J. Menéndez and A. M. Rao, *J. Nanosci. Nanotechnol.*, 2002, **2**, 499–502.
- 65 S. B. Yahia, L. Znaidi, A. Kanaev and J. P. Petitet, *Spectrochim. Acta, Part A*, 2008, **71**, 1234–1238.
- 66 Y. Huang, M. Liu, Z. Li, Y. Zeng and S. Liu, *J. Mater. Sci. Eng. B*, 2003, **97**, 111–116.
- 67 R. S. Yadav and A. C. Pandey, *Struct. Chem.*, 2009, **20**, 1093–1097.
- 68 A. P. Moura, R. C. Lima, M. L. Moreira, D. P. Volanti, J. W. M. Espinosa, M. O. Orlandi, P. S. Pizani, J. A. Varela and E. Longo, *Solid State Ionics*, 2010, **181**, 775–780.
- 69 N. Ashkenov, B. N. Mbenkum, C. Bundesmann, V. Riede, M. Lorenz, D. Spemann, E. M. Kaidashev, A. Kasic,



- M. Schubert, M. Grundmann, G. Wagner, H. Neumann, V. Darakchieva, H. Arwin and B. Monemar, *J. Appl. Phys.*, 2003, **93**, 126–133.
- 70 T. C. Damen, S. P. S. Porto and B. Tell, *Phys. Rev.*, 1966, **142**, 570–574.
- 71 C. A. Arguello, D. L. Rousseau and S. P. S. Porto, *Phys. Rev.*, 1969, **181**, 1351–1363.
- 72 M. Tsuboi and A. Wada, *J. Chem. Phys.*, 1968, **48**, 2615–2618.
- 73 A. Zaoui and W. Sekkal, *Phys. Rev. B: Condens. Matter Mater. Phys.*, 2002, **66**, 1741061–1741066.
- 74 R. Jothilakshmi, V. Ramakrishnan, R. Thangavel, J. Kumar, A. Sarua and M. Kuball, *J. Raman Spectrosc.*, 2009, **40**, 556–561.
- 75 R. Cuscó, E. Alarcón-Lladó, J. Ibáñez, L. Artús, J. Jiménez, B. Wang and M. Callahan, *J. Phys. Rev. B*, 2007, **75**, 165202–165207.
- 76 J. Zhao, X. Yan, Y. Yang, Y. Huang and Y. Zhang, *Mater. Lett.*, 2010, **64**, 569–572.
- 77 L. N. Dem'yanets, D. V. Kostomarov and I. P. Kuz'mina, *Inorg. Mater.*, 2002, **38**, 124–131.
- 78 X. Liu, X. Wu, H. Cao and R. P. H. Chang, *J. Appl. Phys.*, 2004, **95**, 3141–3147.
- 79 N. U. Sangari and S. C. Devi, *J. Solid State Chem.*, 2013, **197**, 483–488.
- 80 A. Becheri, M. Durr, P. L. Nostro and P. Baglioni, *J. Nanopart. Res.*, 2008, **10**, 679–689.
- 81 S. Maensiria, P. Laokula and V. Promarak, *J. Cryst. Growth*, 2006, **289**, 102–106.
- 82 E. F. Venger, A. V. Melnichuk, L. Y. Melnichuk and Y. A. Pasechnik, *Phys. Status Solidi B*, 1995, **188**, 823–831.
- 83 F. Li, L. Hu, Z. Li and X. Huang, *J. Alloys Compd.*, 2008, **465**, 114–119.
- 84 H. X. Niu, Q. Yang, F. Yu, K. B. Tang and Y. Xie, *Mater. Lett.*, 2007, **61**, 137–140.
- 85 X. Jiang, Y. Liu, Y. Gao, X. Zhang and L. Shi, *Particuology*, 2010, **8**, 383–385.
- 86 X. Gao, X. Li and W. Yu, *J. Phys. Chem. B*, 2005, **109**, 1155–1161.
- 87 S. D. Shinde, G. E. Patil, D. D. Kajale, D. V. Ahire, V. B. Gaikwad and G. H. Jain, *Int. J. Smart Sensing and Intell. Systems*, 2012, **5**, 57–70.
- 88 H. Zhang, D. Yang, X. Ma, Y. Ji, J. Xu and D. Que, *J. Nanotechnol.*, 2004, **15**, 622–626.
- 89 X. M. Sun, X. Chen, Z. X. Deng and Y. D. Li, *Mater. Chem. Phys.*, 2002, **78**, 99–103.
- 90 H. Zhang, D. Yang, Y. Ji, X. Ma, J. Xu and D. Que, *J. Phys. Chem. B*, 2004, **108**, 3955–3958.
- 91 U. N. Maiti, S. Nandy, S. Karan, B. Mallik and K. K. Chattopadhyay, *Appl. Surf. Sci.*, 2008, **254**, 7266–7271.
- 92 Y. Liu, H. Lv, S. Li, G. Xi and X. Xing, *Adv. Powder Technol.*, 2011, **22**, 784–788.
- 93 Y. H. Ni, X. W. Wei, X. Ma and J. M. Hong, *J. Cryst. Growth*, 2005, **283**, 48–56.
- 94 J. Ge, B. Tang, L. Zhuo and Z. Shi, *J. Nanotechnol.*, 2006, **17**, 1316–1322.
- 95 X. P. Gao, Z. F. Zheng, H. Y. Zhu, G. L. Pan, J. L. Bao, F. Wu and D. Y. Song, *Chem. Commun.*, 2004, 1428–1429.
- 96 M. Bitenc, G. Drazic and Z. C. Orel, *Cryst. Growth Des.*, 2010, **10**, 830–837.
- 97 B. G. Wang, E. W. Shi and W. Z. Zhong, *Cryst. Res. Technol.*, 1997, **32**, 659–667.
- 98 S. C. Zhang and X. G. Li, *Colloids Surf.*, 2003, 35–44.
- 99 L. N. Dem'yanets, D. V. Kostomarov and I. P. Kuz'mina, *Inorg. Mater.*, 2002, **38**, 124–131.
- 100 C. L. Kuo, T. J. Kuo and M. H. Huang, *J. Phys. Chem. B*, 2005, **109**, 20115–20121.
- 101 B. G. Wang, E. W. Shi and W. Z. Zhong, *Cryst. Res. Technol.*, 1998, **33**, 937–941.
- 102 P. Kubelka and F. Munk-Aussig, *Zeit. Fur. Tech. Physik.*, 1931, **12**, 593–599.
- 103 P. J. A. Porn, S. Suwanboon and P. J. Amornpitoksuk, *J. Ceram. Process. Res.*, 2011, **12**, 85–89.
- 104 Y. Huo and Y. H. Hu, *Ind. Eng. Chem. Res.*, 2012, **51**, 1083–1085.
- 105 R. Rusdi, A. A. Rahman, N. S. Mohamed, N. Kamarudin and N. Kamarulzaman, *Powder Technol.*, 2011, **210**, 18–22.
- 106 S. Suwanboon, P. Amornpitoksuk and S. Muensit, *J. Ceram. Process. Res.*, 2010, **11**, 419–424.
- 107 T. V. Kolekar, H. M. Y. Adav, S. S. A. Bandgar, A. C. Raskar, S. G. Rawal and G. M. Mishra, *Indian Streams Res. J.*, 2011, **2**, 1–3.
- 108 Y. Tong, L. Dong, Y. Liu, D. Zhao, J. Zhang, Y. Lu, D. Shen and X. Fan, *Mater. Lett.*, 2007, **61**, 3578–3581.
- 109 K. F. Lin, H. M. Cheng, H. C. Hsu, L. J. Lin and H. F. Hsieh, *Chem. Phys. Lett.*, 2005, **409**, 208–211.
- 110 D. C. Look, C. R. Donald, J. R. Sizelove, R. L. Jones, C. W. Litton, G. Cantwell and W. C. Harsch, *Solid State Commun.*, 1998, **105**, 399–401.
- 111 A. J. Hauser, J. Zhang, L. Mier, R. A. Ricciardo, P. M. Woodward, T. L. Gustafson, L. J. Brillson and F. Y. Yang, *Appl. Phys. Lett.*, 2008, **92**, 22290.
- 112 J. J. Thevaril and S. K. O'leary, *Solid State Commun.*, 2010, **150**, 1851–18555.
- 113 K. Sakai, T. Kakeno, T. Ikari, S. Shirakata, T. Sakemi, K. Awai and T. Yamamoto, *J. Appl. Phys.*, 2006, **99**, 043508.
- 114 R. E. Marotti, P. Giorgi, G. Machado and E. A. Dalchiele, *Sol. Energy Mater. Sol. Cells*, 2006, **90**, 2356–2361.
- 115 J. Y. Kang, S. Tsunekawa and A. Kasuya, *Acta Phys. Sinica*, 2001, **50**, 2198–2205.
- 116 L. Zhang, L. Yin, C. Wang, N. Lun, Y. Qi and D. Xiang, *J. Phys. Chem. C*, 2010, **114**, 9651–9658.
- 117 U. Koch, A. Fojtik, H. Weller and A. Henglein, *Chem. Phys. Lett.*, 1985, **122**, 507–510.
- 118 L. Brus, *J. Phys. Chem.*, 1986, **90**, 2555–2560.
- 119 P. R. Lucena, F. M. Pontes, C. D. Pinheiro, E. Longo, P. S. Pizani, S. Lázaro, A. G. Souza and I. M. G. Santos, *Ceramica*, 2004, **50**, 138–144.
- 120 G. Blasse and B. C. Grabmaier, *Luminescent Materials*, Springer-Verlag, Berlin, 1994.
- 121 M. Izaki, T. Shinagawa and H. Takahashi, *J. Phys. D: Appl. Phys.*, 2006, **39**, 1481–1484.
- 122 B. D. Yao, Y. F. Chan and N. Wang, *Appl. Phys. Lett.*, 2002, **81**, 757–759.



- 123 A. B. Djurisić, Y. H. Leung, K. H. Tam, Y. F. Hsu, L. Ding, W. K. Ge, Y. C. Zhong, K. S. Wong, W. K. Chan, H. L. Tam, K. W. Cheah, W. M. Kwok and D. L. Phillips, *J. Nanotechnol.*, 2007, **18**, 095702.
- 124 S. Duo, Y. Li, Z. Liu, R. Zhong and T. Liu, *J. Alloys Compd.*, 2017, **695**, 2563–2579.
- 125 L. V. Bora and R. K. Mewada, *Renewable Sustainable Energy Rev.*, 2017, **76**, 1393–1421.
- 126 J. Ni, J. Gao, X. Geng, D. He and X. Guo, *Appl. Phys. A: Mater. Sci. Process.*, 2017, **123**, 186.
- 127 H. Liu, T. Lv, C. Zhu and Zh. Zhu, *Sol. Energy Mater. Sol. Cells*, 2016, **153**, 1–8.
- 128 E. Pervaiz, H. Liu and M. Yang, *Nanotechnology*, 2017, **28**, 105701.
- 129 S. Garcia-Segura and E. Brillas, *J. Photochem. Photobiol., C*, 2017, **31**, 1–35.
- 130 S. G. Kumar and K. S. R. K. Rao, *Appl. Surf. Sci.*, 2017, **391**, 124–148.
- 131 J. Wang, Y. Chen, G. Liu and Y. Cao, *Composites, Part B*, 2017, **114**, 211–222.
- 132 Z. Wang, K. Dai, C. Liang, J. Zhang and G. Zhu, *Mater. Lett.*, 2017, **196**, 373–376.
- 133 Z. Lin, J. Li, Z. Zheng, J. Yan, P. Liu, Ch. Wang and G. W. Yang, *ACS Nano*, 2015, **9**, 7256–7265.
- 134 L. V. Bora and R. K. Mewada, *Renewable Sustainable Energy Rev.*, 2017, **76**, 1393–1421.
- 135 M. Pelaez, N. T. Nolan, S. C. Pillai, M. K. Seery, P. Falaras, A. G. Kontos, P. S. M. Dunlop, J. W. J. Hamilton, J. A. Byrne, K. O'Shea, M. H. Entezari and D. D. Dionysiou, *Appl. Catal., B*, 2012, **125**, 331–349.
- 136 J. G. McEvoy and Z. Zhang, *J. Photochem. Photobiol., C*, 2014, **19**, 62–75.

